

Battery Energy Storage Systems for Primary Frequency Regulation in Power Systems

by

Harindya Shehani Attanayaka

A thesis submitted to the Faculty of Graduate Studies of
The University of Manitoba
in partial fulfilment of the requirements of the degree of

MASTER OF SCIENCE

Department of Electrical and Computer Engineering
University of Manitoba
Winnipeg, Canada

Copyright © 2023 Harindya Shehani Attanayaka

Abstract

Due to the increasing deployment of renewable energy resources, the proportion of conventional power plants is declining. As a result, reduction of frequency-regulation capability has become a significant challenge to be addressed. To mitigate this issue, battery energy storage systems are a favorable candidate owing to their fast response, high energy density, and diversity of battery chemistries.

This thesis provides an improved adaptive state of charge-based droop control strategy for battery energy storage systems participating in primary frequency regulation in a large network. The proposed method has dual features including providing/absorbing power to/from the grid considering state-of-charge, and also enhancing short-term frequency response by giving an additional boost to the droop coefficient to reduce the maximum frequency dip/rise. It also allows batteries with a low state of charge to participate in frequency regulation without risking battery degradation or regulation failure.

The performance of the proposed method is compared with three existing methods and comprehensive simulation studies are conducted to investigate the response of the grid-side and battery-side converter parameters while undergoing multiple contingencies. The proposed frequency regulation method has shown an improved frequency response in terms of maximum frequency dip/rise, compared with frequently utilized methods in the literature.

From the grid's viewpoint, the proposed method is beneficial as it fully utilizes the capacity of the battery energy storage system to support a weak grid with high penetration of renewable energy resources without exhausting the batteries.

Acknowledgements

Foremost, I would like to thank my supervisor Professor Shaahin Filizadeh for his guidance and support throughout the research.

I would like to thank the technical staff of the Department of Electrical and Computer Engineering for the assistance they have given to solve technical issues.

I am very much grateful to my family in Winnipeg for their support and caring during these years. Special thanks go to Prof. Udaya Annakkage, Dilrukshi Annakkage, Dilsha and Buddhi, Githmi and Prabash, and Madushani. Also, I would like to express my gratitude to senior colleagues for showing interest in my work and giving constructive ideas for the success of my research.

I would also like to thank Prof. J.P. Karunadasa and Prof. Lidula N Widanagama Arachchige for the invaluable knowledge and opportunities they have given me.

Last but not least, I would like to extend my gratitude to my family, and friends in Sri Lanka for their encouragement, understanding, and patience throughout my academic pursuit.

Dedications

To my parents and malli

Table of Contents

Abstract	ii
Acknowledgements	iv
Dedications	v
List of Figures	ix
List of Tables	xii
1 Introduction	1
1.1 Background	1
1.2 Problem Definition	3
1.3 Research Objectives	5
1.4 Outline of the Thesis	5
2 Literature Review	7
2.1 Frequency Response of a Power System	7
2.2 Primary Frequency Regulation Techniques	10
2.3 Primary Frequency Regulation by BESS	13
2.4 Dynamic Models of Battery for Frequency Regulation Studies	20
2.5 Chapter Summary	21

3	SOC-based Adaptive droop control method	22
3.1	Overview	22
3.2	Proposed Primary Frequency Regulation Method	24
3.2.1	Calculation of Adaptive SOC-Based Droop Coefficients	24
3.2.2	Validation of the Proposed PFR Method against Existing Methods	29
3.2.3	Enhancement of Short Term Frequency Support to Minimize the Maximum Frequency Dip/Rise	32
3.2.4	Power Plant Controller (PPC) of BESS	34
3.3	Chapter Summary	36
4	Modelling of Battery Energy Storage Systems	37
4.1	Battery Model	37
4.2	DC-DC Converter	39
4.2.1	Detailed Model of DC-DC Converter	39
4.2.2	Average-Value Model of DC-DC Converter	40
4.3	Voltage Source Converter (VSC)	45
4.4	Overall Layout and Control Structure of BESS	48
4.5	Synchronous Generator	50
4.6	Wind Power Plant Model	51
4.7	Chapter summary	52
5	Detailed Assessment	53
5.1	Summary of the Parameters of Models	54
5.2	Assessment of the Proposed PFR method	55
5.3	Case Studies with the IEEE 9-Bus System	59

5.3.1	Case Study 1	60
5.3.2	Case Study 2	64
5.3.3	Case Study 3	68
5.4	Chapter Summary	71
6	Contributions, Conclusions, and Recommendation for Future Work	72
6.1	Contributions and Conclusions	72
6.2	Recommendation for Future Work	74
	References	75
	Appendix A	84

List of Figures

2.1	Frequency response stages stipulated by ENTSO-E [1].	9
2.2	Simplified model of PFR with fixed droop.	15
2.3	Simplified model of PFR with variable droop.	16
2.4	Characteristic curve for conservative strategy [63].	17
2.5	Characteristic curve for radical strategy [63], [65].	18
3.1	Droop characteristics of the BESS.	23
3.2	Variation droop coefficients as a function of SOC.	25
3.3	Flow chart of the proposed adaptive droop control.	27
3.4	Power output variations of BESS with SOC and frequency deviation.	28
3.5	Schematic diagram of a simple test System.	29
3.6	(a) SOC (b) battery power (c) energy consumed by the load	30
3.7	Battery power vs SOC (a) conservative (b) radical (c) proposed method	31
3.8	Variation of modified droop coefficients ($K_{d,mod}$, $K_{c,mod}$) with time.	33
3.9	Block diagram of PPC of BESS.	34
3.10	Controller paths within the PPC.	35
4.1	Shepherd battery model.	39

4.2	Operation of a bidirectional dc-dc converter.	40
4.3	Switching period	42
4.4	Average-value model of a bi-directional dc-dc converter.	43
4.5	(a) DC -link voltage, (b) Inductor current, (c) Duty ratio	44
4.6	A two-level, three-phase VSC.	45
4.7	Model used for derivation of decoupled control.	46
4.8	Decoupled control loops.	48
4.9	Block diagram of the BESS showing its components and controllers.	49
4.10	Synchronous machine model with exciter, governor, and turbine.	51
4.11	Wind power plant model.	52
5.1	Schematic diagram of the test system.	55
5.2	(a) Grid- frequency, (b) BESS power, (c) SG power for step load addition of 45 MW.	57
5.3	Steady state frequency deviation vs SOC for load addition of 15 MW.	58
5.4	(a) Grid- frequency, (b) BESS power for step load reduction of 15 MW.	58
5.5	IEEE 9-bus system with installed BESS, wind power plant, and loads.	59
5.6	Response of frequency at bus 4 for load addition of 15 MW for (a) initial SOC of 0.2 (b) initial SOC of 0.8.	61
5.7	Response of frequency at bus 4 for load tripping of 15 MW for initial SOC of (a) 0.2 and (b) 0.8.	63
5.8	Response of frequency at bus 4 for generation increase of 20% for an initial SOC of (a) 0.2 and (b) 0.8.	65
5.9	Response of frequency at bus 4 for generation reduction of 20% for (a) initial SOC of 0.2 (b) initial SOC of 0.8.	66

5.10	Variations of K_d and $K_{d,mod}$ with time.	69
5.11	(a) Frequency response at bus 4 for load addition of 15 MW (b) battery SOC	70
5.12	Variations of K_d and $K_{d,mod}$ for a load change of 15 MW.	70

List of Tables

2.1	ENTSO-E Network Code [1]	8
2.2	Comparison of North American cases - conventional generation [24]	8
2.3	Characteristics of Different Energy Storage Systems [24, 51–53]	13
2.4	Limitations of Existing PFR Techniques	14
2.5	Key Factors of Droop Control Techniques	19
3.1	Equations for Charge/Discharge of BESS	26
4.1	Battery Cell Parameters	38
4.2	Parameters of bi-directional dc-dc converter	44
5.1	Parameters of the Test System.	54
5.2	Steady state frequency deviation and maximum frequency dip	56
5.3	Case study 1	60
5.4	Comparison of maximum frequency dip for load addition of 15 MW	62
5.5	Comparison of maximum frequency rise for load tripping of 15 MW	62
5.6	Case study 2	64
5.7	Comparison of maximum frequency rise for wind generation increase	66
5.8	Comparison of maximum frequency dip for wind generation reduction	67

5.9	Deviation of SOC	69
A.1	Terminal conditions of IEEE 9-bus system	84
A.2	Transmission line characteristics of IEEE 9-bus system	84
A.3	Load characteristics of IEEE 9-bus system	85
A.4	Synchronous generator parameters	85
A.5	Exciter AC8B parameters	86
A.6	Hydro governor parameters	86
A.7	Hydro turbine parameters	86
A.8	Parameters of PPC	87

Chapter 1

Introduction

1.1 Background

Replacement of conventional generation systems with intermittent renewable energy generation sources has two significant impacts on power systems, namely the reduction of system inertia and instability of the system frequency [1]. Therefore, frequency regulation has become one of the most important challenges in power systems with diminishing inertia [1, 2].

In modern power grids, energy storage systems, renewable energy generation, and demand-side management are recognized as potential solutions for frequency regulation services [1, 3–7]. Energy storage systems, e.g., battery energy storage systems (BESSs), supercapacitors, flywheel energy storage systems, and superconducting magnetic energy storage systems, are considered as the most viable solutions among those alternatives [8]. Distinct energy storage systems have different characteristics, i.e., response time, energy density, power density, lifetime, and efficiency, and the selection of a suitable energy storage system for a particular stage of frequency regulation services must be made incorporating the aforementioned

characteristics [1,9]. It is worth mentioning that BESS is presently dominant for frequency regulation services owing to its high energy density, fast response, low self-discharge rate, and diversity of materials used [1,10,11]. Among different battery chemistries, lithium-ion batteries are considered the most promising technology as they have significant merit factors that outnumber their limitations [1,11].

Conventionally, primary frequency regulation (PFR) methods bring the system frequency to a new steady after a frequency contingency event with complete deployment within 30 seconds [12,13]. Hence, PFR services require continuous power for a relatively long period of time [1]. Thus, BESSs are a favorable candidate for PFR owing to their fast response and high energy capacity; BESS can also balance generation and demand by either absorbing or supplying power based on the requirements of the network. At the present time Hornsdale power reserve in South Australia is the largest lithium-ion BESS with 100 MW/129 MWh ratings and has been operating since 2017 providing two distinct services including energy arbitrage (purchasing low-cost, off-peak energy and selling it during periods of high price) and contingency spinning reserve (fast response to a contingency such as a generation failure) [14]. In 2017, after an unexpected tripping of a large coal power plant, Hornsdale power reserve was able to respond within milliseconds by delivering several megawatts of power to the system, thus preventing a potential cascading blackout [14].

Several theoretical and experimental studies have been conducted to analyze the impact of BESS on PFR based on the improvement of frequency response and economic viability [15–18]. Furthermore, commercially available grid-scale BESSs (> 10.4 MW) for PFR are mentioned in [19], which shows the effectiveness of Li-ion batteries for frequency services. In [20], a hybrid flywheel/battery grid storage solution, developed by Schwungrad Energie Limited, Ireland, to provide variable droop response is presented. In [21] the East Penn

smart grid demonstration project in the US, consisting of battery/ultra-capacitor ESS to provide FR ancillary services, is described.

Furthermore, various BESS control strategies and comprehensive battery models for PFR are proposed in the existing literature with their own limitations and strengths. (This will be further discussed in Chapter 2.) In these approaches, when developing a PFR method, special attention has been given to maintaining the state of charge (SOC) of the battery within the pre-defined limits to preserve the lifetime of the battery. Therefore, in most cases, BESS is to be operated in the frequency regulation phase as well as the SOC recovery phase. If priority is given to the SOC recovery phase, it can negatively impact the effectiveness of the frequency regulation phase [10, 22]. Therefore, the penalty cost due to regulation failure will be increased.

1.2 Problem Definition

The International Energy Agency has predicted that renewable energy generation will become the largest contributor to the world's energy generation portfolio giving a total of one-third of the world's energy demand by 2025 and is expected to reach 45% by 2040 [23]. Even though the utilization of renewable energy generation gives rise to multiple economic and environmental benefits, it poses challenges to the power system including instability of system frequency and output intermittency.

A power system with high penetration levels of renewable energy generations has a high Rate of Change of Frequency (RoCoF), which leads to large frequency nadirs within a short period of time even for a small mismatch between generation and demand. A large frequency nadir may lead to unintended load shedding or even the collapse of the system if sufficient

frequency regulation capacity is not present. Therefore, an important aspect of future power grids with high renewable penetration levels is to hold the frequency above the load shedding limit for considerably longer periods until non-spinning reserves are brought into service.

Many methods including the utilization of energy storage systems and de-loading of renewable energy generations are presented to mitigate the above issues by providing frequency regulation services. However, modern power systems with high penetration levels of renewable energy generation essentially operate at maximum power point and, as mentioned earlier, grid operators are leaning towards further increasing the level of non-synchronous generation. Therefore, de-loading of renewable energy generations to provide frequency regulation is not technically and economically viable. As such, energy storage systems, which can solve the issue of intermittency of renewable energy sources and also provide ancillary support are the most suitable candidate to address these problems.

Consequently, it is necessary to select a proper type of energy storage system and develop its control strategy to provide a particular type of ancillary support. Grid-scale BESS is considered as the dominant energy storage system, which can cover a wide time frame including short-term frequency regulation (i.e., PFR) and long-term frequency regulation (i.e., secondary frequency regulation).

Therefore, to fully harness the potential of batteries for a prolonged time, suitable frequency regulation control strategies must be selected, which improve the system frequency response and do not exhaust the batteries. Especially, PFR techniques, which supply power for relatively short periods of time, may require considering the energy capacity and SOC of batteries to ensure battery availability for additional grid support services including secondary frequency regulation or contingency spinning. On the other hand, it is worth noting that the existing SOC-based PFR methods have solely focused on maintaining SOC within

pre-defined limits instead of prioritizing frequency regulation services. From a system point-of-view, it is disadvantageous, especially when the power system consists of a high level of renewable energy generation and less conventional generation. Therefore, a PFR method that has a proper balance between providing PFR regulation services and maintaining battery SOC is required. Therefore, in this research, effort has been made to develop an improved PFR regulation method for grid-scale BESS considering SOC and the energy capacity of batteries.

1.3 Research Objectives

The objectives of this research are listed below.

- Implementation of a dynamic model of a Li-ion battery incorporating its SOC along with detailed and average-value models of dc-dc converters and voltage source converter (VSC) in an EMT simulator (PSCAD/EMDTC).
- Development of an improved adaptive SOC-based droop control for BESS participating in PFR and performance evaluation of the proposed control strategy using the IEEE 9-bus system while the system undergoes multiple contingencies.

1.4 Outline of the Thesis

A general background of BESS participating in PFR was described in this chapter. Chapter 2 presents a comprehensive literature review on the frequency response of a power system, an outline of different PFR techniques including their drawbacks, different PFR techniques of

BESS proposed in the literature along with their limitations, and dynamic models of battery for frequency regulation.

Chapter 3 describes the proposed adaptive SOC-based PFR method including the calculation of adaptive droop control coefficients and integration of the proposed PFR method to the power plant controller of BESS.

Modeling of BESS along with its controllers and other components is presented in Chapter 4. A dynamic model of a battery, detailed and average-value models of a bidirectional dc-dc converter, voltage source converter (VSC), synchronous generator, and wind farm are developed with their controls.

Chapter 5 presents detailed analysis of the proposed PFR method. To observe its response, a test system that consists of a BESS, fixed loads, and a synchronous generator is developed on PSCAD/EMTDC. The contribution of heterogeneous batteries for PFR and variation of steady state frequency deviation with battery SOC is observed for two distinct load change events. Also to exhibit the effectiveness of the proposed PFR method in terms of improved frequency response, it is compared with frequently employed approaches mentioned in the literature, when the BESS is connected to the IEEE 9-bus system. A summary of system parameters and corresponding values is also presented.

Conclusion, contributions, and suggestions for future work are given in Chapter 6.

Chapter 2

Literature Review

In this chapter, an overview of the frequency response of a power system with increasing penetration of renewable energy generation, the utilization of different PFR techniques involving energy storage systems and renewable energy generation, the suitability of BESS for providing PFR, and various models and control strategies of BESS for PFR are discussed.

2.1 Frequency Response of a Power System

Frequency is one of the key measures that reflects the stability of a power system. Any mismatch between the demand and generation causes fluctuations in frequency. A surplus of generation results in an increase in frequency, while a deficit of generation causes a reduction in frequency. To obtain stable operation, it is necessary to maintain the frequency within permissible limits to reduce the likelihood of generation and load disconnections.

There are various sets of frequency regulation standards defined by different system operators for nominal and contingency events. The frequency operating standards defined by the European Network of Transmission System Operator for Electricity (ENTSO-E) are

given in Table 2.1.

Table 2.1: ENTSO-E Network Code [1]

	Great Britain (GB)	The continental Europe (CE)	The inter-Nordic system (NE)	The all-island Irish system (IRE)
Standard frequency deviation range	± 0.2 Hz	± 0.05 Hz	± 0.1 Hz	± 0.2 Hz
Maximum instantaneous frequency deviation	0.8 Hz	0.8 Hz	0.8 Hz	0.8 Hz
Maximum steady state frequency deviation	0.5 Hz	0.2 Hz	0.5 Hz	0.5 Hz
Frequency recovery range	± 0.5 Hz	not used	not used	± 0.5 Hz
Time to recover frequency	60 s	not used	not used	60 s
Frequency restoration range	± 0.2 Hz	not used	± 0.1 Hz	± 0.2 Hz
Time to restore frequency	600 s	900 s	900 s	1200 s

Table 2.2 shows the North American frequency standard defined by North America Electric Reliability Corporation (NERC).

Table 2.2: Comparison of North American cases - conventional generation [24]

Region	Deadband (mHz)	Droop	Response time requirement	Minimum Duration
Global	36	5% (3% - 5%)	5s (0.2 - 10s)	N/A
United States	<36	<5%	No undue delay	Sustained
Texas, US	<34 (steam/hydro) <17 (all other)	4% -5%	14s-16s	30s
New England, US	<36	4% -5%	No undue delay	Sustained
PJM, US	<36	<5%	No undue delay	Sustained
Ontario, Canada	<36	2% -5%	<1s (activation time)	10s

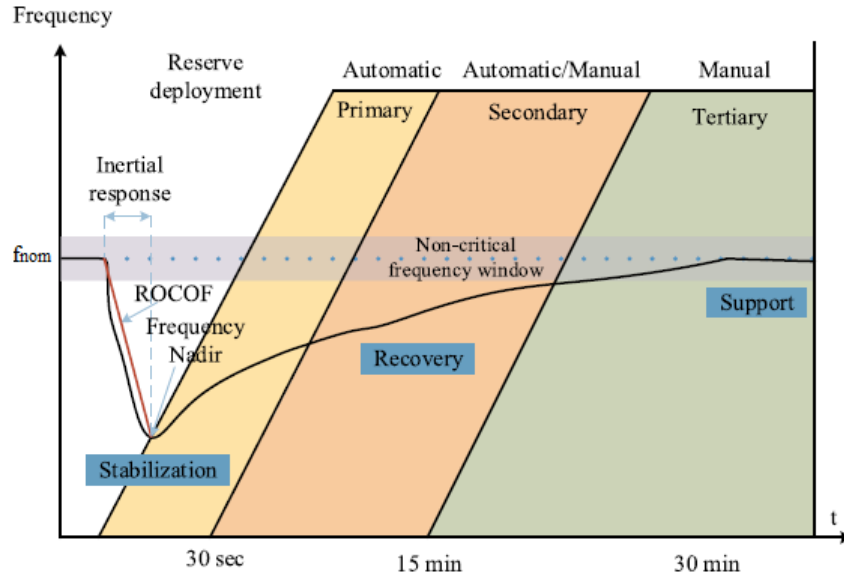


Figure 2.1: Frequency response stages stipulated by ENTSO-E [1].

In conventional power systems, synchronous generators instantaneously and naturally, i.e., without control or measurements, speed-up/slow-down by absorbing/providing the energy from/to the power system in the event of a mismatch of generation and demand [25]. Typical variations of frequency after the occurrence of an event and necessary actions to mitigate the frequency deviation are shown in Figure 2.1. In a conventional power system, during frequency events, synchronous generators improve frequency dynamics by releasing/absorbing kinetic energy stored in their rotating masses. This inherent characteristic is called inertial response (IR). It typically lasts for up to 10 s, which depends on the characteristics of the system. This stage is followed by the primary frequency regulation, which stabilizes the frequency to a new steady state value within tens of seconds (typically within 30 s). Secondary frequency regulation removes the steady-state deviation that emerges after PFR and restores the frequency back to its nominal value over a period of 30s–30 min [13].

In modern power systems with few synchronous generators, applications of several alter-

natives including renewable energy generations (wind turbine and solar photovoltaic), loads using demand side management, and energy storage systems for frequency regulation services have been investigated [23, 26]. Among them, energy storage systems are shown to be an effective solution to improve the frequency response thanks to their fast response and substantial storage capacity [27].

In particular, utility-scale BESSs are frequently employed as operating reserves and provide ancillary services that operate on distinct timescales, ranging from seconds to hours. Since batteries can charge/discharge rapidly, they are convenient for short-term ancillary services such as PFR. Therefore, power-frequency droop control of BESS has shown remarkable improvement in PFR services [28, 29]. It is worth noting that an appropriately-sized BESS can participate in longer-duration services as well. However, many stakeholders may not have fully realized the capabilities of BESS including the ability of a single BESS to provide multiple services. Employing a properly-designed multi-functioned BESS in a modern power system with diminishing conventional generation is particularly valuable from an economic standpoint.

2.2 Primary Frequency Regulation Techniques

This section provides an outline of different PFR techniques in the presence of renewable energy generation along with the strengths and limitations of each technique. Many studies have been conducted to explore the use of variable-speed wind turbine generators for PFR services. To do so, variable-speed wind turbine generators (e.g., doubly-fed induction generators) must be operated in a de-rated manner and provide less power output than the available power [3]. It ensures the availability of a spinning reserve to provide active power

in case of a frequency contingency event. De-loading is divided into two types, namely delta mode and balanced mode [30]. In delta mode, the output is reduced by a defined percentage of the available power, while in balanced mode the output power is decreased by a fixed value. Frequently-employed de-loading is realized by pitching the blades [31]. By doing so, the reference power to the pitch controller is adjusted to a specific value to achieve a targeted de-loading level [32, 33].

Most studies have adopted a droop control method to provide PFR by wind turbines, which is again divided as static droop and variable droop control [34, 35]. Static droop control is similar to the conventional synchronous generator governor control, which supplies active power based on frequency deviation [36]. In the variable droop control method, the dead-band slope can be adjusted according to the de-loading level and wind speed. It is stated that this method improves the frequency response while reducing extra structural loading and it allows each wind turbine to participate in PFR based on its own available power reserve according to the local wind speed [35]. Despite these improvements, the aforementioned PFR methods using wind turbines depend on the variation of wind speed, which is uncertain, and suffer from other limitations mentioned in Table 2.4, Therefore, to mitigate these issues, implementation of ESS is proposed [37].

In the current literature, frequently utilized PFR methods using solar power plants include de-loaded control [5–7, 38, 39] and delta power control [40]. In de-loaded control, the PV system contributes to the PFR by operating away from its maximum power point. The aim is to keep a portion of the PV output as reserve such that whenever there is an increase in load power, the reserve power can be used for frequency regulation. In [5] and [41], the traditional droop control is included in the control loop to adjust the PV power according to the frequency deviation. An adaptive de-loading technique is introduced in [42] allowing

the PV plant to adjust its output power according to rapid frequency deviations. Delta power control is another method of PFR, which allows a certain set of PV panels to operate at maximum power point while others are de-loaded to create a reserve. The operating point is adjusted to limit the PV power output, which leads to delta power production. The limitations of the above-mentioned methods are listed in Table 2.4.

Energy storage systems participate in PFR by absorbing/providing power from/to the grid according to the frequency deviation [1]. Frequently employed energy storage systems are super-capacitors (SCs), flywheel energy storage systems (FESSs), superconducting magnetic energy storage systems (SMESs), and BESS [43–45]. The characteristics of energy storage systems for frequency regulation are given in Table 2.3.

Super-capacitors have the characteristics of electrochemical batteries and traditional capacitors. To achieve high performance, the capacitance of a super-capacitor can be enhanced by utilizing nano-materials to increase the surface area of its electrode [46]. In [47], super-capacitors participate in PFR and secondary frequency regulation according to an adaptive generalized predictive control. However, due to high power density and high efficiency, it is best suited for short-term rather than long-term power applications [48].

A flywheel energy storage system is an electromechanical storage device, which stores energy in the form of the kinetic energy of a rotating mass [49]. It has a rotating cylinder coupled with an electrical machine, which acts as a motor and generator during charging and discharging, respectively. A droop control method based on the SOC of the flywheels is proposed in [50] for wind-flywheel systems to participate in PFR and it is stated that the contribution of the flywheel has reduced the requirement of wind turbines to operate in the de-loaded mode. However, flywheels have low energy density making it difficult to operate them as a standalone energy storage system.

Table 2.3: Characteristics of Different Energy Storage Systems [24, 51–53]

Technology	Power density (MW/m ³)	Energy density (kWh/m ³)	Energy cost (\$/kWh)	Cycle efficiency(%)	Life cycles
FESS	1- 2.5	20-100	1000-14000	90 -95	20000 - 100000
Li- ion batteries	0.4 - 2	200-600	240 -2500	90 -97	up to 20000
SMES	1 - 4	20-100	1000 -10000	95-98	20000 -100000
SCs	0.4 -10	4-100	500 - 15000	90 -97	50000 - 1000000

2.3 Primary Frequency Regulation by BESS

The most frequently-utilized PFR applications of BESS are rule-based control strategies, model predictive control, and droop control methods (fixed droop and variable droop methods). It is worth mentioning that advanced control schemes, namely model predictive and rule-based controls, give better performance, at the expense of complexity and computational burden [1].

In [16], a rule-based control method, which adjusts the limits of SOC based on a statistical analysis of frequency measurements, is proposed for BESS to provide PFR. The main objective of this method is to optimally determine the capacity of the battery to maximize the profit for the owner. Therefore, the impact of this method on grid frequency has not been fully considered. A state-machine-based control strategy for BESS participating PFR is described in [57] to support wind power plants and instead of allowing the battery SOC to vary between maximum and minimum limits, it is controlled to operate at an optimal value

Table 2.4: Limitations of Existing PFR Techniques

Platform		Limitations
Wind Turbine [3, 4, 30, 54–56]		<ul style="list-style-type: none"> • Speed recovery phase, especially under low wind speed conditions, causes frequency secondary dip. • Influence of error in wind speed measurement can negatively influence frequency regulation especially when defining the de-loading ratio and setting the reference rotational speed. Therefore, some wind turbines may become unstable due to a lack of sufficient reserve margin while providing PFR support. • Special actions should be taken in the event of insufficient wind speed; i.e; over-loading the wind turbine. • Wind energy is wasted because of de-loading or/and during the recovery phase after providing power for frequency regulation. • An appropriate de-loading ratio must be selected to achieve maximum power, otherwise, the capacity factor can be reduced. • Overloading techniques, intensive rotational speed control, and pitch de-loading reduce the lifetime of the wind turbine. • The cost due to wind power curtailment causes a negative impact on wind farm revenue.
Solar PV [5–7, 38, 39]		<ul style="list-style-type: none"> • Inadequate de-loading may cause system to become unstable in a frequency contingency event. • Excessive de-loading puts unnecessary burden on grid planners in terms of economics. • Requirement of additional solar strings, temperature, and irradiance sensors will put a burden on economics on solar revenue. • De-loading is not yet suitable for large-scale grids. • PV system cannot participate in under-frequency events when being operated at PV power curtailment.
ESS [1, 46, 48]	SC	<ul style="list-style-type: none"> • Daily self-discharge rate and capital cost is high. • Energy density is relatively low.
	FESS	<ul style="list-style-type: none"> • Energy cost is high. • Energy density is relatively low. • High self-discharge rate.
	SMES	<ul style="list-style-type: none"> • Energy cost is high. • Energy density is relatively low.

(i.e., SOC of 50%) to preserve the battery life.

Droop control, which is simple and easy to implement, is commonly adopted for PFR. It regulates the battery's power output according to the frequency deviation as in conventional synchronous generators [58], [9]. Droop control methods are mainly divided into two groups:

- Fixed droop control methods

As shown in Figure 2.2, a fixed droop control method has a linear relationship between the frequency and the power output of the BESS [1]. In Figure 2.2, f_{grid} is the grid frequency, and f_{nom} is the nominal frequency. A dead band is applied to ensure that PFR is supplied only after the frequency deviation ($f_{\text{grid}} - f_{\text{nom}}$) exceeds a pre-defined value (e.g., ± 0.003 pu). P_{ref}^* is the plant's reference set point and P_{POI} is the measured power at the point of interconnection. R_{bess} is the droop coefficient. The droop coefficient of conventional generators is normally set at 0.04 or 0.05 pu. P_{max} and P_{min} are the maximum and minimum power limits.

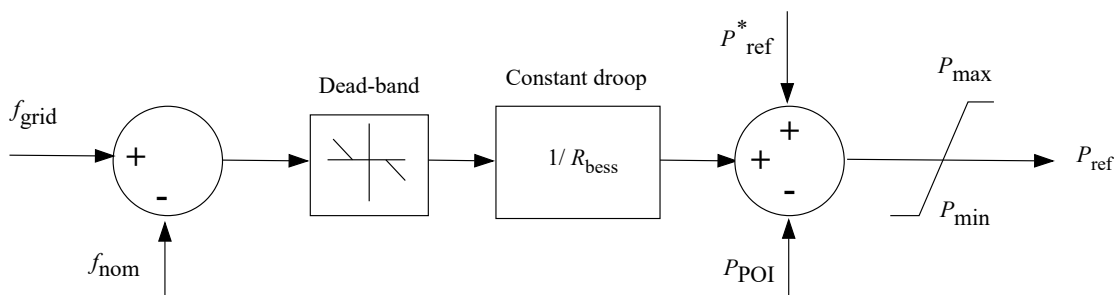


Figure 2.2: Simplified model of PFR with fixed droop.

In [59, 60], the conventional droop control method is implemented to size a single BESS. In [61], conventional droop control with adjustable droop coefficients, adjustable

maximum/minimum power, and adjustable dead-band is proposed for a 1 MW BESS to provide frequency regulation for the islands of Hawaii.

- Variable droop control methods

With a fixed droop control method, during under-frequency events, the BESS can reach the minimum SOC limit while over-frequency events could make BESS reach the maximum SOC limit. Therefore, overcharge/over-discharge may occur leading to battery degradation [62]. As shown in Figure 2.3, a variable droop control method takes the battery’s SOC into consideration to avoid such scenarios. $R_{\text{bess}}(\text{SOC})$ is the variable droop coefficient.

In [62–64], several modified droop control methods with distinct droop coefficients for charging/discharging are proposed for BESS providing PFR. The main focus of these approaches is to preserve battery life by allowing batteries with high SOC to give more power and batteries with low SOC to give less power during a discharging event. Frequently-utilized variable droop control methods, namely conservative and radical methods, are detailed below.

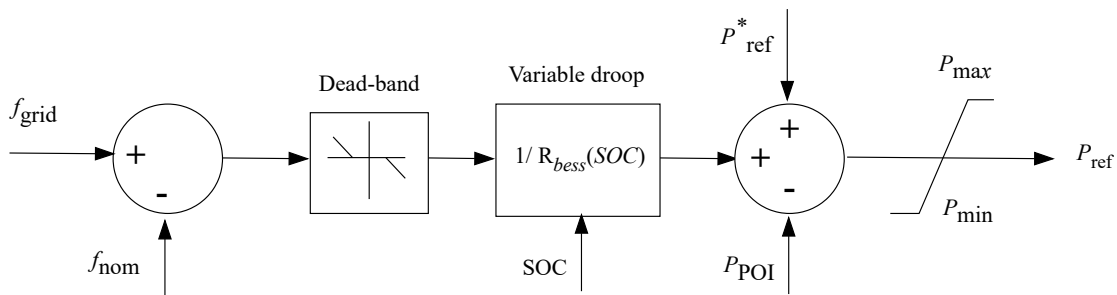


Figure 2.3: Simplified model of PFR with variable droop.

1. Conservative strategy

The Conservative strategy proposes a control method based on available SOC in the battery as shown in (2.1).

$$K = K_{\max} * \begin{cases} SOC^2 & \Delta f \leq 0 \\ (1 - SOC)^2 & \Delta f > 0 \end{cases} \quad (2.1)$$

where K_{\max} is the maximum droop value and K is the droop coefficient. Figure 2.4 shows the relationship between the droop coefficient and SOC. It pays attention to SOC , which allows more power output when SOC is high and less power output when it is low.

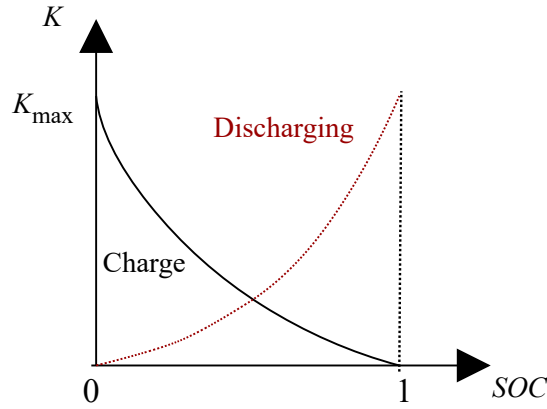


Figure 2.4: Characteristic curve for conservative strategy [63].

2. Radical strategy

As shown in Figure 2.5, the radical strategy uses maximum SOC (SOC_{\max}), minimum SOC (SOC_{\min}), as well as high SOC (SOC_{high}) and low SOC (SOC_{low}) to

limit the power output of the battery. The charging curve is concave down (decreasing) within SOC_{low} and SOC_{max} and the discharging curve is concave down (increasing) within SOC_{min} and SOC_{high} .

In [63], for SOC_{high} and SOC_{low} , values of , 20% and 80% are employed to preserve the lifetime of the battery.

$$K = K_{max} * \begin{cases} (1 - (\frac{SOC - SOC_{high}}{SOC_{min} - SOC_{high}})^2) & \Delta f \leq 0 \\ (1 - (\frac{SOC - SOC_{low}}{SOC_{max} - SOC_{low}})^2) & \Delta f > 0 \end{cases} \quad (2.2)$$

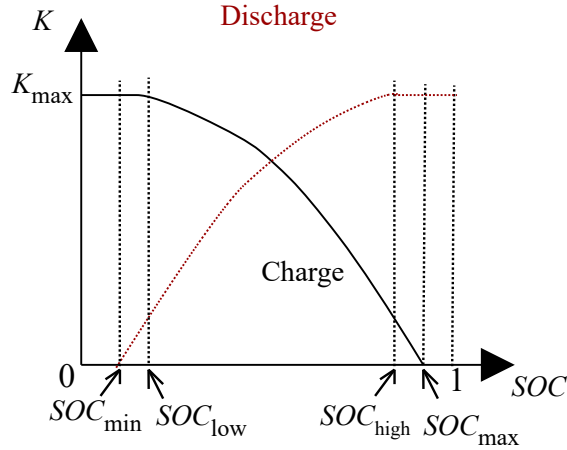


Figure 2.5: Characteristic curve for radical strategy [63], [65].

Table 2.5 shows the key factors of the above mentioned droop control strategies. Even though allowing the battery to provide less power when SOC is low is favorable from the battery's point of view, the system may suffer from a lack of frequency regulation capacity

during severe contingency events. It may lead to under-frequency load shedding and activation of RoCoF relays. Therefore, in this thesis, an adaptive SOC-based droop control method is proposed, which incorporates the merits of both conservative strategy and radical strategy. It accommodates several subsections of SOC to present more variation to the droop coefficients within these intervals.

It should be noted that, in this thesis, SOC_{\max} and SOC_{\min} are considered as 0.9 and 0.1 and they are not the maximum (i.e., 1.0) and minimum SOC (i.e., 0) levels that a battery can reach regardless of considering battery longevity.

Table 2.5: Key Factors of Droop Control Techniques

Method		Key Factors
Fixed droop method		This method does not consider the influence of SOC of batteries on droop coefficient. Therefore, battery over-charging/over-discharging can occur.
Variable droop method	Conservative strategy	During charging process, from 0 to 1, the decrease rate of K_c also decreases and during discharging process, the increase rate of K_d increases. Even though this method changes K_c and K_d according to SOC, it prioritizes maintaining SOC instead of supplying/absorbing more power to/from the grid.
	Radical strategy	During charging process, from SOC_{low} to SOC_{\max} , the decrease rate of K_c increases, and during discharging process, from SOC_{\min} to SOC_{high} , the increase rate of K_d decreases. This method is an improved method of conservative strategy. As opposed to the conservative method, during the charging period, at high SOC, it absorbs more power and during discharging period, at low SOC, it supplies more power.

2.4 Dynamic Models of Battery for Frequency Regulation Studies

Several battery models with different merits and limitations have been proposed for frequency regulation services, including a Thevenin model, non-linear Shephard model, first-order lag model [66], first-order lag model with SOC [67], battery equivalent circuits with converter [68], and incremental BESS model [69, 70].

With a voltage source, a series resistance, and a parallel RC branch, the Thevenin model represents the dynamic behavior of a battery to a large extent. Adding more RC branches can improve the dynamic response, but due to the compromise between complexity and computational cost, it is not suitable for frequency regulation services [71]. In [72], a Thevenin model is employed for PFR studies, the SOC's dependence on battery parameters is ignored. First-order lag models and first-order lag models with SOC are often used for frequency regulation services, especially for secondary frequency regulation studies.

In [66], a first-order lag model is utilized to evaluate the performance of a PI controller for frequency regulation in a solar thermal-diesel-wind hybrid renewable system. The objective of [66] is to optimize the PI controllers' gains in the hybrid system. In [67], a first-order lag model with SOC is used to suppress frequency deviations in wind power generation and the performance of the proposed method is simulated using a two-area Load Frequency Control (LFC) model. Even though only one parameter (time constant) is required, internal characteristics are represented in neither of the above-mentioned models. In [68], the BESS is represented using a converter connecting an equivalent battery where the battery is represented as a capacitance and equivalent resistance. However, an RC parallel branch is added to describe the energy and voltage variations during charging or discharging; SOC

dependence is not considered. An incremental model is similar to the battery equivalent circuits and is widely used in Load Frequency Control studies [69]. The only difference is that in the incremental BESS model, the terminal voltage of the battery is not considered an input signal.

In [73], the battery is represented as a voltage source in series with a resistor. However, the dynamics of the dc-dc converter and voltage source converters are not considered; the effect of SOC is not included. The adopted battery model in this research is the Shephard model, which describes the electrochemical behavior of a battery in terms of its terminal voltage, open circuit voltage, internal resistance, charge/discharge current, and SOC [74]. This model is further discussed in Chapter 4.

2.5 Chapter Summary

It is evident that future power grids will be equipped with more renewable sources and less conventional generation. Therefore, if the application of BESS is proposed as an ancillary service (i.e., PFR), it is important to hold the frequency above load-shedding limits for a considerably long period by using BESS, until non-spinning reserves are brought into service. Among various PFR techniques of BESS, the variable droop control strategy is considered as a simple and easy method to implement. An essential feature to have in these variable droop control methods is the proper balance between providing PFR service and maintaining the SOC of batteries. Since prioritizing balancing SOC instead of participating in PFR can lead to regulation failure, it will increase the penalty cost assessed for regulation failure.

Chapter 3

SOC-Based Adaptive Droop Control Method

3.1 Overview

In this chapter, a comprehensive description of the proposed PFR method and its key features are discussed. As the initial step, an overview of the operation of grid-connected BESS providing PFR is presented here.

Figure 3.1 shows the active power-frequency droop characteristics of the BESS. It also depicts the variation of discharging droop coefficient (K_d) and charging droop coefficient (K_c) between 0 and the maximum droop coefficient (K_{\max}).

P_{\max} is the maximum charging/discharging power, Δf_{\max} is the maximum frequency deviation, K_{\max} is the maximum droop coefficient, and Δf_{db} is the dead-band within which the BESS remains idle; Δf is the frequency deviation at a given time; f_m is the measured grid frequency and f_{nom} is the nominal grid frequency. With the change in the SOC of

batteries, K_d and K_c vary between 0 and K_{\max} . The relationship between power-frequency for charging/discharging is given in (3.1), (3.2) and (3.3) .

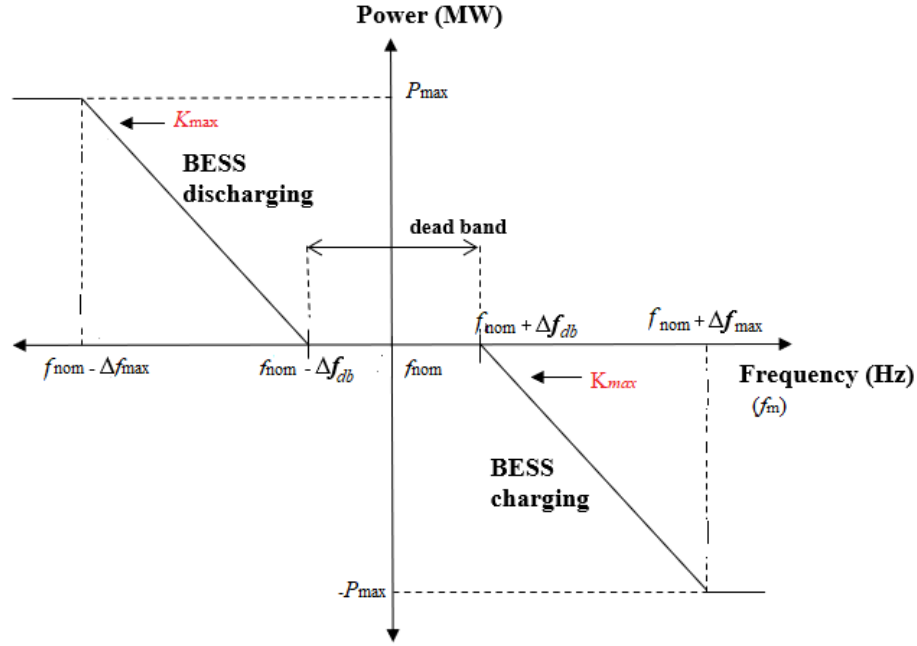


Figure 3.1: Droop characteristics of the BESS.

$$\Delta f = f_m - f_{\text{nom}} \quad (3.1)$$

$$K_{\max} = \frac{P_{\max}}{\Delta f_{\max} - \Delta f_{\text{db}}} \quad (3.2)$$

$$P_{\text{BESS}} = \begin{cases} (-\Delta f + \Delta f_{\text{db}}) * K_c, & (f_{\text{nom}} + \Delta f_{\text{db}}) < f_m < (f_{\text{nom}} + \Delta f_{\max}) \\ -(\Delta f + \Delta f_{\text{db}}) * K_d, & (f_{\text{nom}} - \Delta f_{\text{db}}) > f_m > (f_{\text{nom}} - \Delta f_{\max}) \\ 0, & 0 \leq |f_m - f_{\text{nom}}| \leq \Delta f_{\text{db}} \\ P_{\max}, & |f_m - f_{\text{nom}}| \geq \Delta f_{\max} \end{cases} \quad (3.3)$$

In Section 3.2.1, mathematical expressions for K_d and K_c within the intervals of SOC and the way they influence the power output of the BESS are discussed.

3.2 Proposed Primary Frequency Regulation Method

In this section, the calculation of adaptive droop coefficients based on SOC, validation of the proposed droop control method against existing variable droop control strategies, enhancement of short-term frequency support to reduce maximum frequency dip/rise, and integration of the proposed PFR method in the power plant controller (PPC) of the BESS are discussed.

3.2.1 Calculation of Adaptive SOC-Based Droop Coefficients

The method proposed in this thesis is a hybrid of the conservative and radical strategies and gives different droop coefficients for various subsections of SOC curve (see Figure 3.2). The equations for the proposed SOC-based droop control are shown in Table 3.1. Regulation of the charging/discharging process of BESS according to the SOC-based droop coefficient is further explained below.

For a particular battery, SOC_{max} and SOC_{min} are defined and given as inputs to the algorithm. As mentioned earlier SOC_{max} and SOC_{min} are 0.9 and 0.1. In an under-frequency event and if the battery SOC is above SOC_{max} , to provide maximum power the battery will be discharged with maximum droop coefficient, which is K_{max} . From SOC_{max} to SOC_{mid} (which is $(SOC_{max} + SOC_{min})/2$), when SOC decrease, K_d decreases, although the decrease rate of K_d is comparatively low. From SOC_{mid} to SOC_{min} , K_d decreases rapidly. If the SOC is below SOC_{min} , the corresponding battery will not be discharged to prevent over-discharging.

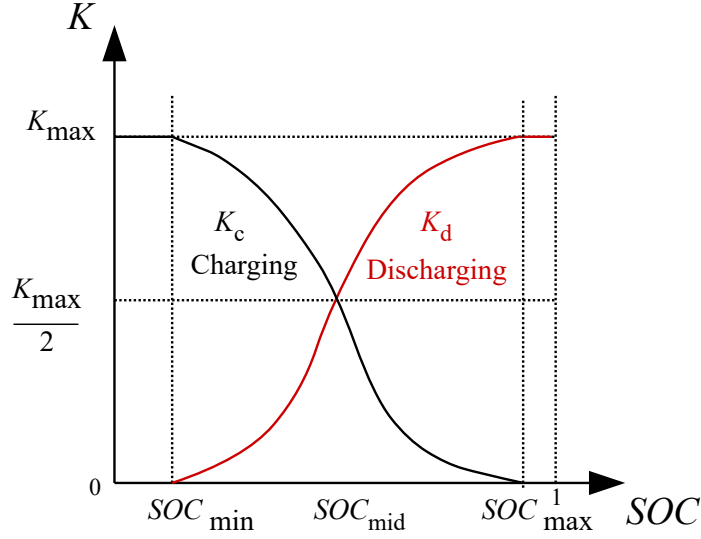


Figure 3.2: Variation droop coefficients as a function of SOC.

In an over-frequency event, if the battery SOC is below SOC_{\min} , the corresponding battery will be charged with maximum droop coefficient, which equals K_{\max} . From SOC_{\min} to SOC_{mid} , when the SOC increases K_c decreases; the decrease rate of K_d is low. From SOC_{mid} to SOC_{\max} , K_c decreases, although the decrease rate of K_c is fast. If the SOC is above SOC_{\max} , the battery will not be charged to prevent over-discharging. Figure 3.3 shows the flowchart of the adaptive droop control method with corresponding inputs and outputs.

As shown in Figure 3.3, if the frequency deviation is within the dead-band (Δf_{db}) no battery will be charged or discharged, and if the frequency deviation is greater than or equal to the maximum deviation (Δf_{\max}) the battery will be charged or discharged giving maximum power regardless of battery SOC. If $|\Delta f|$ is within $[\Delta f_{\text{db}}, \Delta f_{\max}]$, the amount of power the battery is required to supply/store is calculated.

Table 3.1: Equations for Charge/Discharge of BESS

Discharging	Charging
if $SOC \leq SOC_{min}$ $K_d = 0$	if $SOC \leq SOC_{min}$ $K_c = K_{max}$
if $SOC_{min} \leq SOC \leq \frac{(SOC_{min} + SOC_{max})}{2}$ $K_d = 2K_{max} \left(\frac{SOC_{max} - SOC}{SOC_{max} - SOC_{min}} \right)^2$	if $SOC_{min} \leq SOC \leq \frac{(SOC_{min} + SOC_{max})}{2}$ $K_c = K_{max} \left(1 - 2 \left(\frac{SOC - SOC_{min}}{SOC_{max} - SOC_{min}} \right)^2 \right)$
if $\left(\frac{SOC_{max} + SOC_{min}}{2} \right) \leq SOC \leq SOC_{max}$ $K_d = K_{max} \left(1 - 2 \left(\frac{SOC - SOC_{min}}{SOC_{max} - SOC_{min}} \right)^2 \right)$	if $\left(\frac{SOC_{max} + SOC_{min}}{2} \right) \leq SOC \leq SOC_{max}$ $K_c = 2K_{max} \left(\frac{SOC_{max} - SOC}{SOC_{max} - SOC_{min}} \right)^2$
if $SOC \geq SOC_{max}$ $K_d = K_{max}$	if $SOC \geq SOC_{max}$ $K_c = 0$

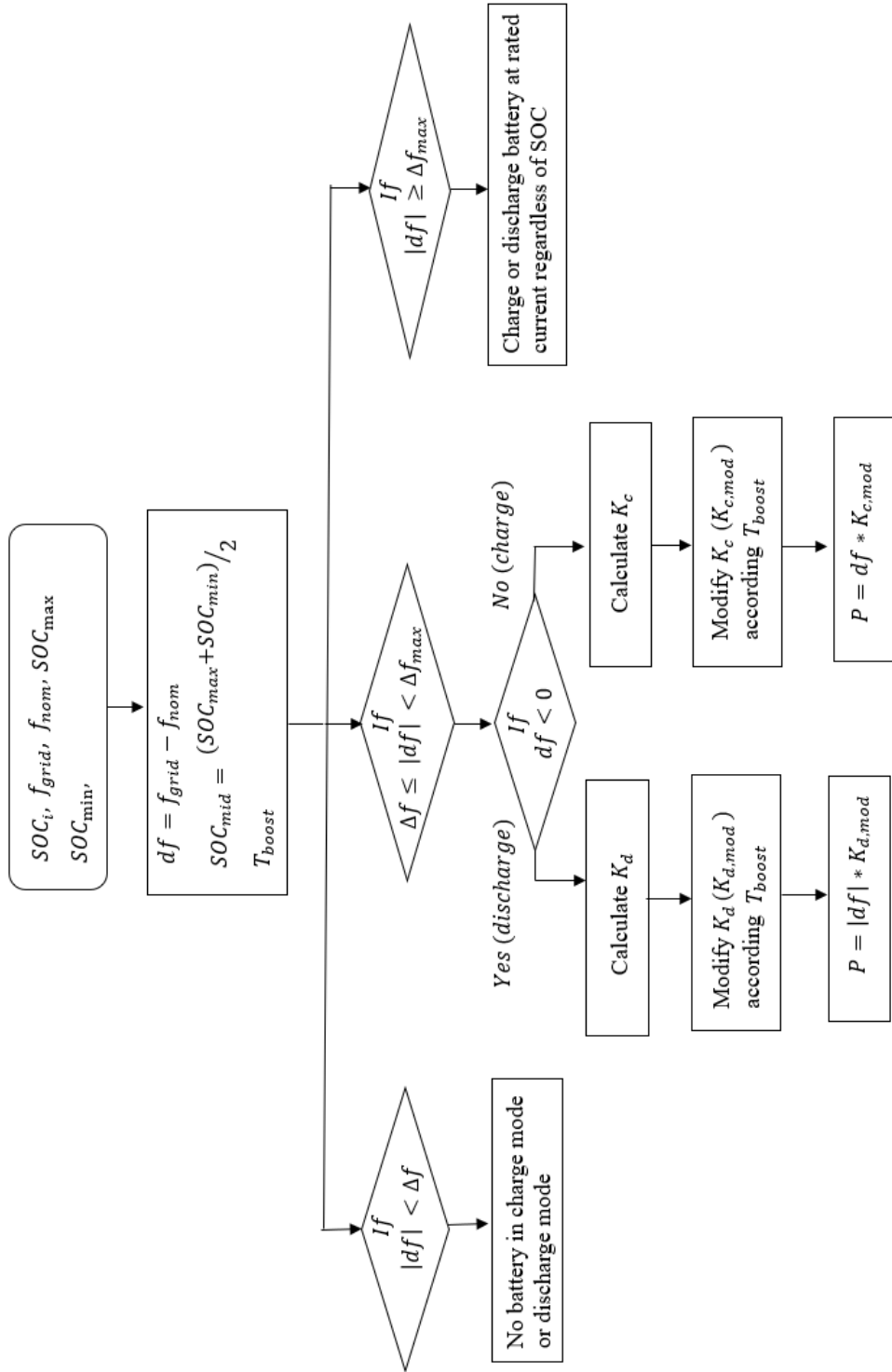


Figure 3.3: Flow chart of the proposed adaptive droop control.

To observe this, the test system shown in Figure 3.4(a) with a BESS of 0.85 MW, 0.5kAh interfaced to an ac system is considered. For different SOC and frequency deviation (Δf) values, the output power of the battery, (P_b), is measured. Δf_{max} and Δf_{db} values are 0.15 Hz and 0.01 Hz.

When the frequency is within the dead band, BESS is idle absorbing/giving no power from/to the grid. During the charging period, when SOC increases, the amount of power absorbed by the battery decreases. During the discharge period, when SOC decreases, the amount of power supplied by the battery also decreases (see Figure 3.4(b)).

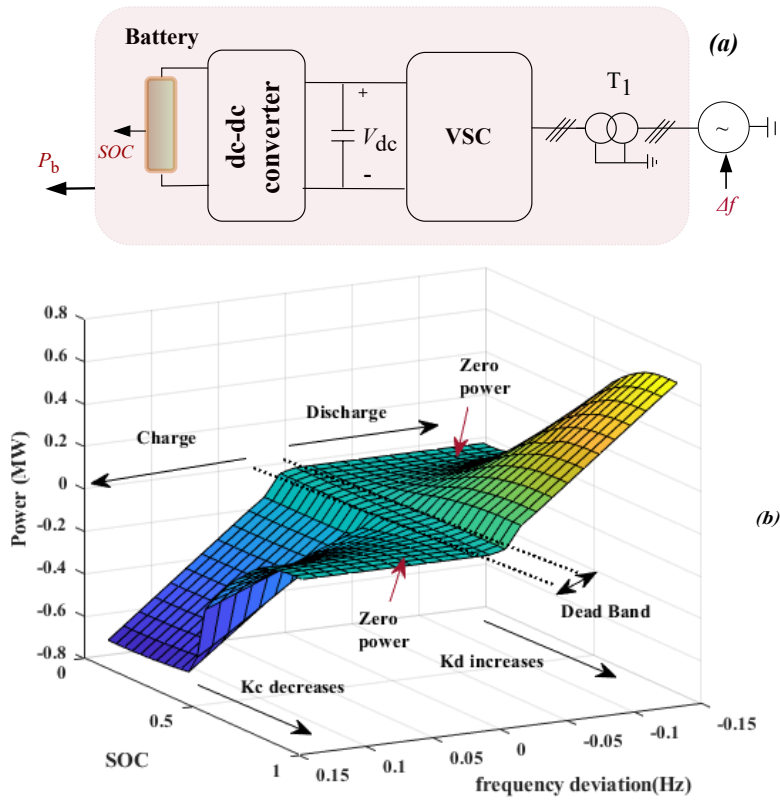


Figure 3.4: Power output variations of BESS with SOC and frequency deviation.

3.2.2 Validation of the Proposed PFR Method against Existing Methods

In this section, the behavior of three algorithms (the proposed method, conservative strategy, and radical strategy) are tested for given frequency deviations on the grid side. The main objective of this study is to observe the variations of SOC and the output power given by each method.

A test system with a battery (0.5 kAh, initial SOC of 1.0 (i.e. 100%)) is considered to which a variable resistive load is connected as shown in Figure 3.5. The detailed modeling of the battery and calculation of battery SOC is presented in Chapter 4. The variable resistive load is a simple representation of the inverter as seen by the battery. The initial transients of the frequency of the ac system (not modeled) are not considered. In this test system, a situation where the system is settled at a 2% (i.e., 1.2 Hz) of persistent frequency dip (Δf) is considered in order to observe the behavior of different droop algorithms. A detailed study including the dynamics of BESS for frequency deviations due to multiple contingencies is given in Chapter 5.

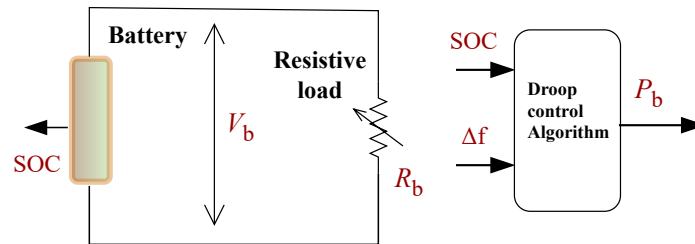


Figure 3.5: Schematic diagram of a simple test System.

Inputs to the droop control algorithm are SOC and frequency deviation (Δf). V_b is the battery's terminal voltage which is 1.9 kV and P_b is the required power calculated by the

droop controller. The resistive load value is calculated below.

$$R_b = \frac{V_b^2}{P_b} \quad (3.4)$$

Figure 3.6 shows the variation of battery SOC, power, and energy consumed by the load for each droop control strategy. Conservative strategy is more concerned about preserving SOC, therefore it gives less power, and the variation of SOC is also less compared to the other methods. The radical strategy gives more power without considering the level of SOC, and consequently the reduction of SOC is more. The proposed method combines the merits of the conservative strategy and radical strategy by giving more output power when SOC is relatively high (as the radical strategy) and preserving the battery SOC by giving less power when SOC is relatively less (as the conservative strategy).

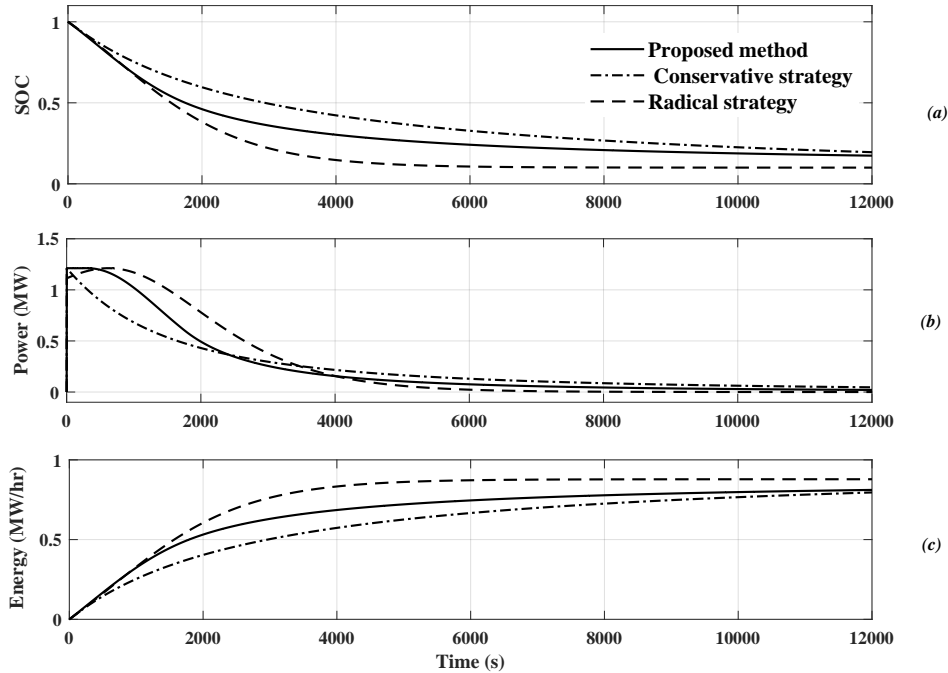


Figure 3.6: (a) SOC (b) battery power (c) energy consumed by the load

Figure 3.7 shows the variation of battery power with SOC for all three strategies and they are similar to the characteristic curves mentioned in 2.3.

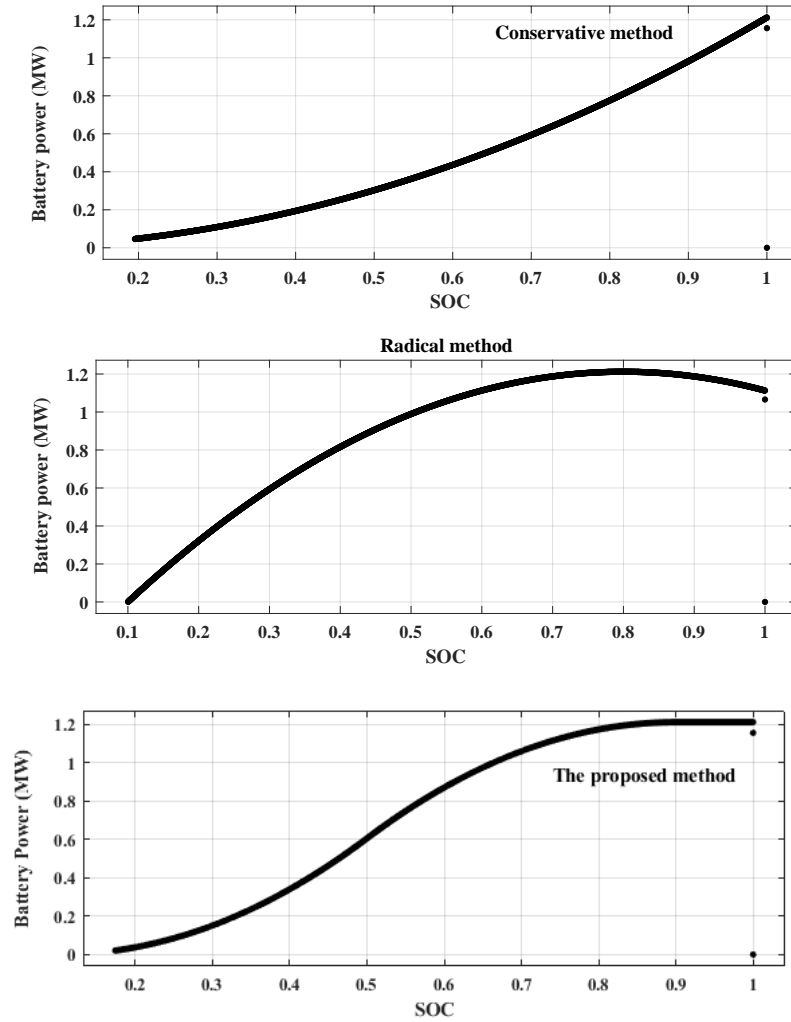


Figure 3.7: Battery power vs SOC (a) conservative (b) radical (c) proposed method

3.2.3 Enhancement of Short Term Frequency Support to Minimize the Maximum Frequency Dip/Rise

One limitation of the proposed method is during an under-frequency event, it will provide maximum power to the grid only when the battery's SOC is greater than SOC_{\max} . From the system's viewpoint, this is unfavorable, because a grid-scale BESS with high energy capacity can support the grid by providing maximum power even with lower-than-maximum SOC for a small period of time. Likewise, a BESS with SOC higher than the minimum can be charged at maximum droop coefficient (K_{\max}) for short time period.

Further explaining this, in a discharging scenario, K_{\max} is only achievable when the SOC is at SOC_{\max} ; for any SOC below SOC_{\max} , K_d will be less than K_{\max} . As a result if the BESS observes an under-frequency event when it is not at a fully charged state (i.e, SOC is less than SOC_{\max}), then the initial power given by BESS is determined by a K_d value that is less than the K_{\max} .

This can be improved if the BESS is always set to operate at the K_{\max} value for a short interval of time, disregarding the SOC, whenever a frequency event is triggered. Also, the value of the droop coefficient can be slowly brought down to the value determined by the droop curve (K_d) with time. The duration of this interval can be determined by considering the SOC. A similar modification may be applied to the charging coefficient as well. The advantage of this improvement is that due to the additional boost given to the droop coefficients (i.e., K_d and K_c) the maximum frequency dip/rise will be reduced. The process is explained below.

1. As the first step, the time duration of the boosted action (T_{boost}), when the battery supplies/absorbs power to/from the grid after a disturbance, is calculated based on the

SOC, P_{\max} , and the maximum energy capacity (E_{\max}) of the battery.

$$T_{\text{boost}} = \frac{E_{\max} * SOC}{P_{\max}} \quad (3.5)$$

2. Then, K_d (or K_c) is modified into $K_{d,\text{mod}}$ (or $K_{c,\text{mod}}$) as below. It should be noted that K_d and K_c are calculated according to the equations in Table 3.1.

$$K_{d,\text{mod}} = \frac{K_{\max} - K_d}{\left(e^{\left(\frac{t - T_{\text{boost}}}{2}\right)} + 1\right)} + K_d \quad (3.6)$$

$$K_{c,\text{mod}} = \frac{K_{\max} - K_c}{\left(e^{\left(\frac{t - T_{\text{boost}}}{2}\right)} + 1\right)} + K_c \quad (3.7)$$

Figure 3.8 shows the variation of modified droop coefficients ($K_{d,\text{mod}}$, $K_{c,\text{mod}}$) with time. T_{bd} is the time it takes the frequency to exceed the dead band value.

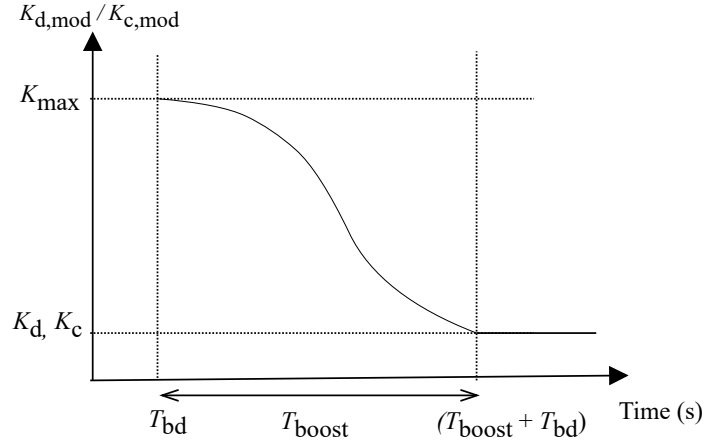


Figure 3.8: Variation of modified droop coefficients ($K_{d,\text{mod}}$, $K_{c,\text{mod}}$) with time.

With this modification, the power system is supported by the BESS during the initial

stage of disturbance by operating at the K_{\max} . By doing so, it will prevent the frequency from exceeding standard limits; accordingly unscheduled load shedding and activation of RoCoF relays can be avoided. The advantage of modified droop coefficients is presented in section 5.3.3. It will show how the grid frequency is improved in terms of maximum frequency dip and how it does not negatively impact SOC.

3.2.4 Power Plant Controller (PPC) of BESS

Previous sections of this chapter discussed the development of the proposed PFR method. This section presents the integration of the proposed PFR method to the PPC of BESS.

As shown in Figure 3.9, the battery SOC is an input to the PPC from the battery. System frequency (f_{POI}) is measured using a phase-locked loop (PLL). Active power (P_{POI}), reactive power (Q_{POI}), and the RMS voltage ($V_{\text{POI,rms}}$) at the point of interconnection (POI) are the other inputs to the PPC. The outputs of the PPC are the active power command (P_{ref}) and reactive power command (Q_{ref}) (discussed in Section 4.4).

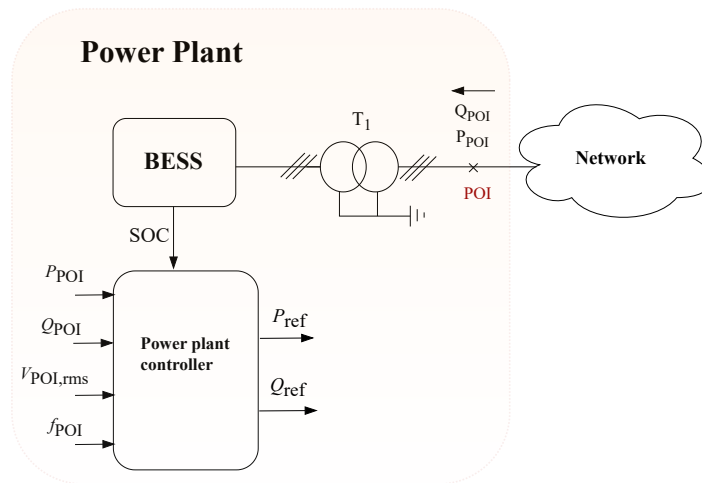


Figure 3.9: Block diagram of PPC of BESS.

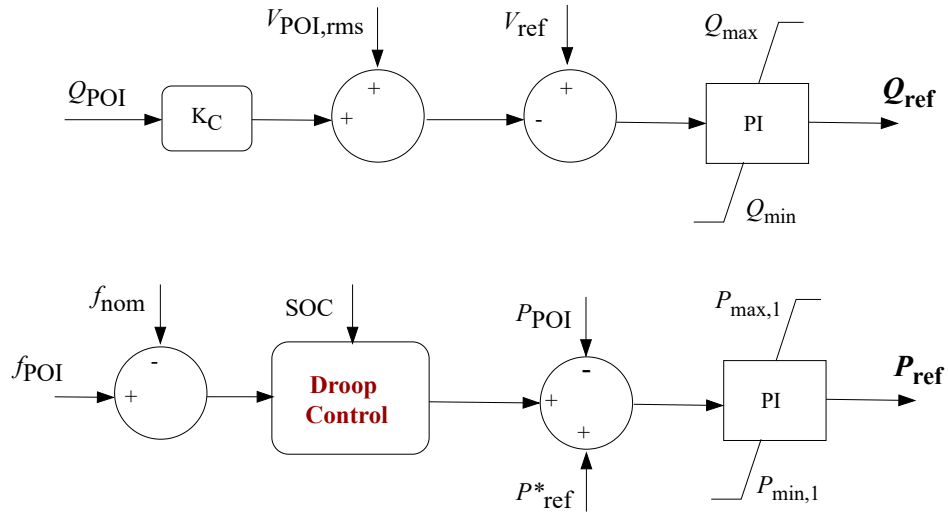


Figure 3.10: Controller paths within the PPC.

As shown in Figure 3.10, the generic renewable plant control model in PSS/E (REPCA1) is modified by adding the proposed adaptive SOC-based droop algorithm. f_{nom} is the nominal grid frequency, V_{ref} is the reference voltage and P^*_{ref} is the power plant's reference set point. $P_{max,1}$ and $P_{min,1}$ are the upper and lower limits of the power reference, respectively. In this scheme, the PPC injects reactive power proportional to the voltage deviation at POI. Q_{max} and Q_{min} are the upper and lower limits on the output of the V/Q control; K_C is the reactive power compensation gain.

The values of corresponding parameters for simulation studies are shown in Appendix A.

3.3 Chapter Summary

It can be concluded that the proposed adaptive SOC-based variable droop control method has dual features of providing/absorbing power to/from the grid based on battery SOC and improving short-term frequency response by giving an additional boost to the droop coefficients. The proposed method consists of the merits of the often-employed variable droop PFR techniques (i.e., conservative strategy and radical strategy). The merits are: during an under-frequency event, when SOC is high, it supplies more power as the radical strategy and when SOC is low, it gives less power as the conservative strategy. The integration of the proposed method into the PPC of BESS is presented with corresponding controllers.

Chapter 4

Modelling of Battery Energy Storage Systems

4.1 Battery Model

The battery model employed for this study is the Shepherd model, selected due to its reasonably high accuracy and simplicity [74]. In this model, the electrochemical behavior of a battery is described in terms of the terminal voltage, open circuit voltage, internal resistance, and discharge current/charge current. The expression in (4.1) describes a lithium-ion battery model.

$$V_{\text{batt}} = E_0 - Ri - K \frac{Q}{Q - \int i(t)dt} + Ae^{-B \int i(t)dt} \quad (4.1)$$

where

V_{batt} = battery voltage (V)

E_0 = battery nominal voltage (V)

K = Polarisation constant (VAh⁻¹) or polarisation resistance (Ω)

Q = Battery capacity (Ah)

A = Exponential zone amplitude (V)

B = Exponential zone time constant inverse (Ah⁻¹)

R = Internal resistance (Ω)

$i(t)$ = Battery current (A)

It is assumed that the internal resistance (R) is constant during charging and discharging and does not depend on the SOC and other battery temperature. Self-discharge of the battery is not taken into consideration. Battery parameters are extracted from discharge characteristics and are assumed to be the same for charging as well. The Li-ion battery cell parameters in [74] and shown in Table 4.1 are adopted in this study.

Table 4.1: Battery Cell Parameters

Parameter	Li-ion cell (3.3 V, 2.3 Ah)
E_0 [V]	3.336
R (Ω)	0.01
K (Ω)	0.0076
A [V]	0.26422
B [Ah ⁻¹]	26.5487

SOC calculation method

In this study, the Coulomb counting method is used to calculate the battery's SOC. In this method, as shown in (4.2), the SOC is calculated by accumulating the charge flowing in or out of the battery [11].

$$SOC = SOC_0 - \frac{\eta}{C_{\text{rated}}} \int idt \quad (4.2)$$

where SOC_0 is the initial SOC and C_{rated} is the rated capacity. The Coulomb counting method can be improved by considering Coulombic efficiency. It is defined as the ratio of

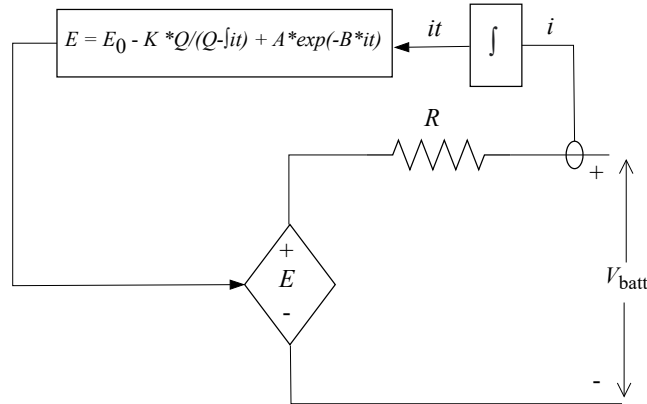


Figure 4.1: Shepherd battery model.

the discharging capacity to the charging capacity. As it depends on the current rate (discharge or charge), an equivalent Coulombic efficiency (η) is developed including discharge Coulombic efficiency and charge Coulombic efficiency. Since Li-ion batteries offer high equivalent Coulombic efficiency, η is taken as 0.99 in this study [11].

4.2 DC-DC Converter

A bidirectional dc-dc converter is implemented to step up/down the output voltage of the battery. It is employed to achieve power transfer in both directions. Commonly used bidirectional dc-dc converter models are detailed models and average value models, which will be further discussed.

4.2.1 Detailed Model of DC-DC Converter

During the discharging process, the converter operates in boost mode as shown in Figure 4.2(a). During the charging process, as shown in Figure 4.2(b), the converter operates in

buck mode.

The converter is operated by sending firing pulses to MOSFETs Q_1 and Q_2 . The duty cycle (D) is generated using a proportional-integral (PI) controller and is compared with a triangular carrier waveform to generate the gate pulses to Q_1 and Q_2 .

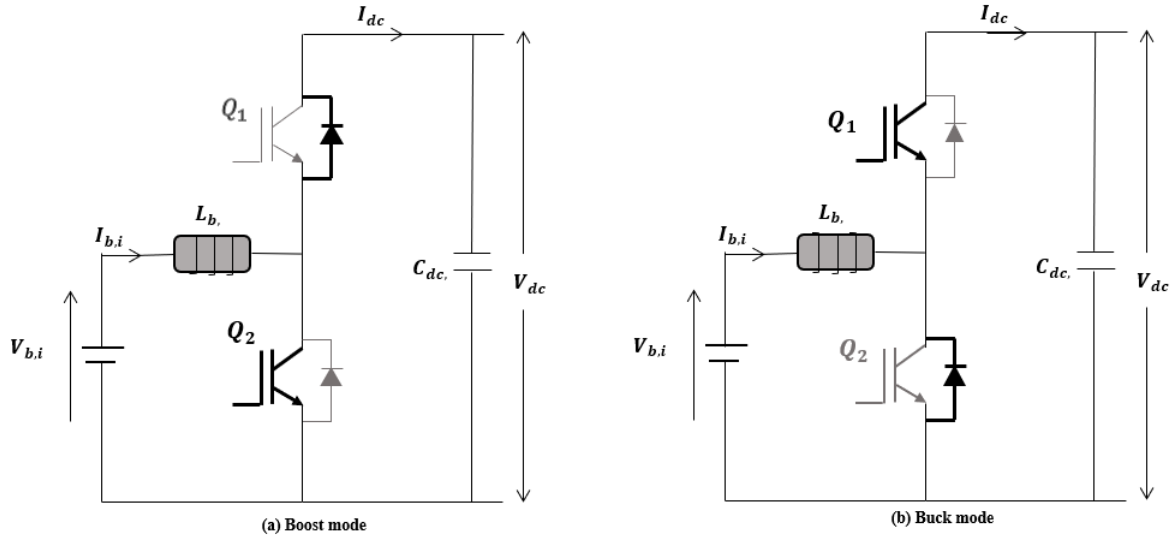


Figure 4.2: Operation of a bidirectional dc-dc converter.

4.2.2 Average-Value Model of DC-DC Converter

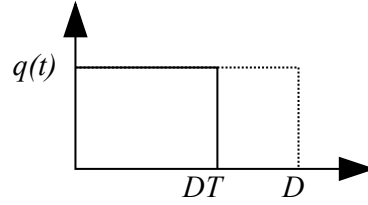
The detailed modeling of power-electronic converters includes switches and pulse-width modulation, whose models are available in simulation tools including PSCAD/EMTDC. These models require a small simulation time step, which will increase the computational time. To mitigate these problems, several average-value models have been developed in the literature [75].

Average value models of power-electronic converters are developed neglecting or “averaging” the effects of fast-switching action. In the existing literature, two general methods

of averaging are proposed, namely state-space modeling and averaged-switch modeling [75]. In state-space averaging, the system's state equations are derived for various switching combinations and then averaged using appropriate weightings that depend on the duration of time the converter dwells in each switching state [76]. On the contrary, in averaged-switch modeling, the switched-inductor cell is represented by appropriate dependent current and voltage sources [77].

Several improved average-value models in existing literature are full-order models and reduced-order models, which consider duty ratio constraints, the effect of losses, and parasitics to construct a particular model. The representation of the effects of parasitics and losses adds complexities to analytical derivations [78]. Also, it leads to nonlinear current/voltage waveforms. Often the effect of parasitics is included in the process of circuit averaging method. The effectiveness of the modification to the ideal switched-inductor cell depends on the mode of the operation [79]. It is worth mentioning that modifying state-space equations to account for the losses and effects of parasitics complicates the task of average-value modeling [80]. Therefore, with these complexities, the application of such models to large systems increases the computation time. Therefore, a simple average-value model for system-level studies of the larger system without compromising accuracy is derived. The model is represented using controlled current sources and voltage sources, which are functions of duty ratio.

Consider the boost mode of operation of the bidirectional converter (see Figure 4.2(a)). The duty ratio of Q_2 is D and T is the switching period (see Figure 4.3). Two conditions for the switch Q_2 are considered.

**Figure 4.3:** Switching period

Q_2 is ON:

$$q(t) = 1 \quad (4.3)$$

$$\frac{di_L}{dt} = \frac{1}{L}V_{in} \quad (4.4)$$

$$\frac{dV_{dc}}{dt} = \frac{1}{C_{dc}}\left(\frac{-V_{dc}}{R}\right) \quad (4.5)$$

Q_2 is OFF:

$$q(t) = 0 \quad (4.6)$$

$$\frac{di_L}{dt} = \frac{1}{L}(V_{in} - V_{dc}) \quad (4.7)$$

$$\frac{dV_{dc}}{dt} = \frac{1}{C_{dc}}\left(i_L - \frac{V_{dc}}{R}\right) \quad (4.8)$$

Combining the above equations yields:

$$\frac{di_L}{dt} = \frac{1}{L}(V_{in} - (1 - q(t))V_{dc}) \quad (4.9)$$

$$\frac{dV_{dc}}{dt} = \frac{1}{C_{dc}}\left(i_L(1 - q(t)) - \frac{V_{dc}}{R}\right) \quad (4.10)$$

By averaging the equations (4.9) and (4.10) over a period T , averaged differential equations

can be obtained as (4.11) and (4.12).

$$\frac{di_L}{dt} = \frac{1}{L}(V_{in} - (1-d)V_{dc}) \quad (4.11)$$

$$\frac{dV_{dc}}{dt} = \frac{1}{C_{dc}}(i_L(1-d) - \frac{V_{dc}}{R}) \quad (4.12)$$

It should be noted that the equations are valid for the buck mode as well, and are based upon the assumption that $q(t)$ varies much faster than V_{dc} and i_L .

Using (4.13) and (4.14), the equivalent circuit shown in Figure 4.4 is constructed, where

$$V_{avg} = (1-d)V_{dc} \quad (4.13)$$

$$i_{avg} = (1-d)i_L \quad (4.14)$$

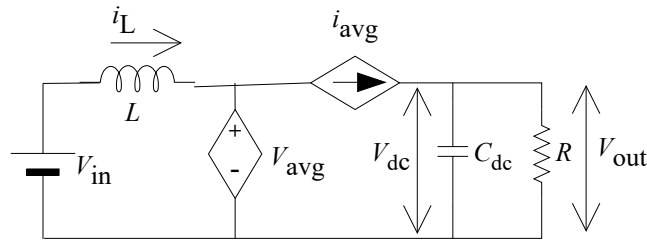


Figure 4.4: Average-value model of a bi-directional dc-dc converter.

To demonstrate the accuracy of the shown model, a bi-directional dc-dc converter is modeled using detailed and average-value approaches. Table 4.2 shows the parameters of the converter. At $t = 8$ s, a 10% load change (0.01445Ω) is given to both models to observe their performance during the transient period. As shown in Figure 4.5 the dc-link voltage, inductor current, and duty ratio produced by the average-value model follow the

corresponding waveforms of the detailed model. High-frequency switchings are visible in the detailed model whereas in the average model they are neglected. The simulation time step is $20\mu\text{s}$.

Table 4.2: Parameters of bi-directional dc-dc converter

Parameter	Value
Output voltage (V_{out})	1.9 kV
Input voltage (V_{in})	1.0 kV
Inductance (L)	1.5 mH
DC-link capacitor (C)	7000 μF
Resistive load (R)	1.445 Ω

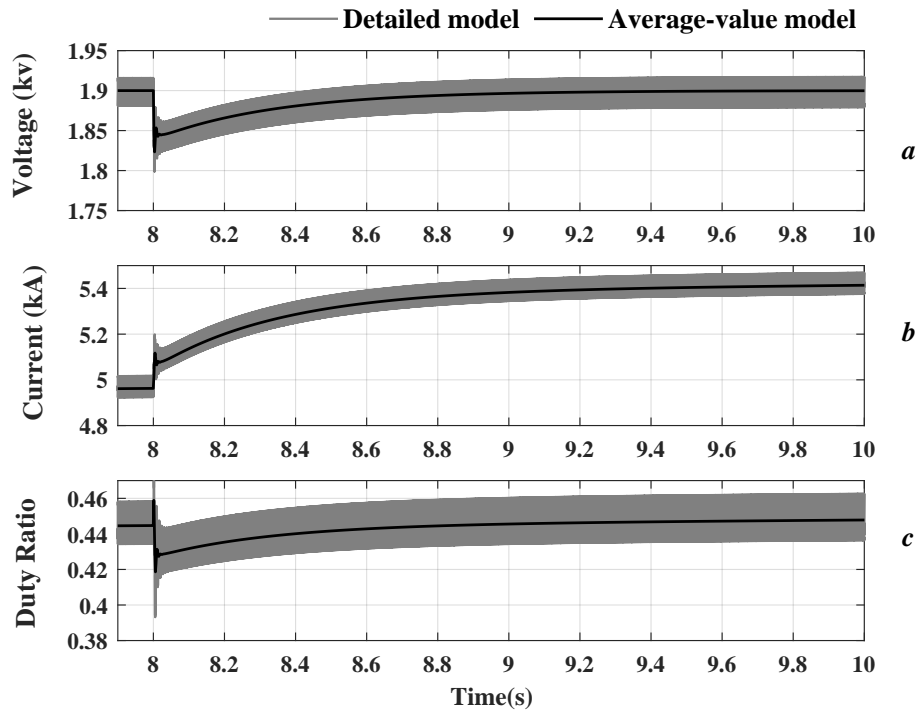


Figure 4.5: (a) DC -link voltage, (b) Inductor current, (c) Duty ratio

4.3 Voltage Source Converter (VSC)

A two-level voltage source converter (VSC) is used to convert dc power to ac power and vice versa. As shown in Figure 4.6, there are two switches in each phase of a two-level VSC, of which only one is on at a given time; it is connected to the ac grid through filters and a transformer. Firing pulses are generated using PWM and a decoupled method is employed to control power exchange between the VSC and the grid.

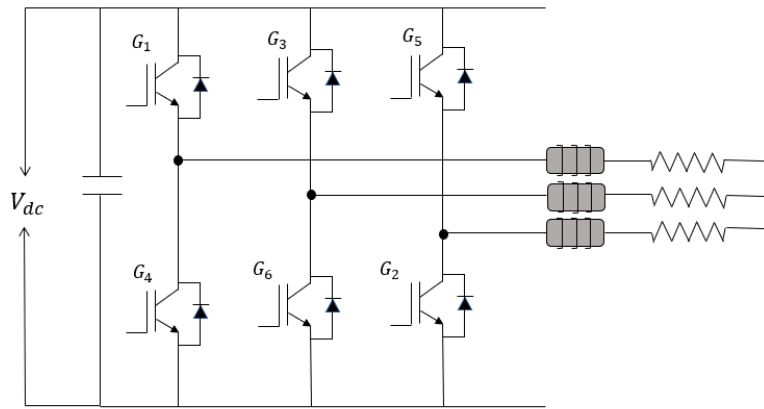


Figure 4.6: A two-level, three-phase VSC.

Decoupled Control of VSC

In decoupled control, to regulate the active power (P) and reactive power (Q), Park's transformation from the abc domain to dq0 domain for the phase voltages and currents is adopted. Park's transformation matrix, T , is shown in (4.15) and dq0 to abc transformation is shown in (4.16).

$$T = \begin{pmatrix} \cos(\theta) & \cos(\theta - \frac{2\pi}{3}) & \cos(\theta + \frac{2\pi}{3}) \\ \sin(\theta) & \sin(\theta - \frac{2\pi}{3}) & \sin(\theta + \frac{2\pi}{3}) \\ \frac{1}{2} & \frac{1}{2} & \frac{1}{2} \end{pmatrix} \quad (4.15)$$

$$X_{qd0} = TX_{abc} \quad (4.16)$$

where θ is an arbitrarily selected value.

System equations in the abc domain for the simple system in Figure 4.7 may be written as follows.

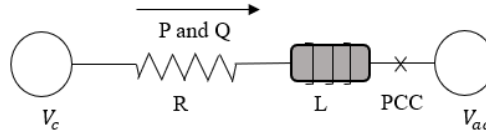


Figure 4.7: Model used for derivation of decoupled control.

$$V_c = Ri_{abc} + L \frac{d}{dt} i_{abc} + V_{ac} \quad (4.17)$$

$$V_{c(qd0)} = TV_{c(abc)} = TL \frac{d(T^{-1}i_{qd0})}{dt} + TRT^{-1}i_{qd0} + V_{ac(qd0)} \quad (4.18)$$

$$V_{c(qd0)} = Ri_{qd0} + TL \frac{d(T^{-1}i_{abc})}{dt} + L \frac{di_{qd0}}{dt} + V_{ac(qd0)} \quad (4.19)$$

$$V_{cq} = Ri_q + \omega_0 Li_d + L \frac{di_q}{dt} + V_{ac,q} \quad (4.20)$$

$$V_{cd} = Ri_d - \omega_0 Li_q + L \frac{di_d}{dt} + V_{ac,d} \quad (4.21)$$

Calculating the active and reactive power in the dq0 domain yields.

$$P = \frac{3}{2}(V_{ac,d}i_d + V_{ac,q}i_q) \quad (4.22)$$

$$Q = \frac{3}{2}(V_{ac,q}i_d - V_{ac,d}i_q) \quad (4.23)$$

It is assumed that the phase angle of the PCC voltage is the reference in this study. V_m is the

peak of the voltage of the phase voltage at PCC and three-phase voltages can be described below.

$$V_{ac,a} = V_m \cos(\omega t) \quad (4.24)$$

$$V_{ac,b} = V_m \cos\left(\omega t - \frac{2\pi}{3}\right) \quad (4.25)$$

$$V_{ac,c} = V_m \cos\left(\omega t + \frac{2\pi}{3}\right) \quad (4.26)$$

With a properly locked PLL:

$$V_{ac,q} = V_m \quad V_{ac,d} = 0 \quad (4.27)$$

Therefore,

$$P = \frac{3}{2} V_m i_q \quad (4.28)$$

$$Q = \frac{3}{2} V_m i_d \quad (4.29)$$

Finally,

$$\frac{di_q}{dt} = \frac{-R}{L} i_q - \omega_0 i_d + \frac{1}{L} (V_{cq} - V_m) \quad (4.30)$$

$$\frac{di_d}{dt} = \frac{-R}{L} i_d + \omega_0 i_q + \frac{1}{L} V_{cd} \quad (4.31)$$

Therefore, as shown in (4.28) and (4.29), active power (P) is regulated by controlling i_q , while reactive power (Q) is regulated using i_d . Decoupled control loops are then obtained as shown in Figure 4.8.

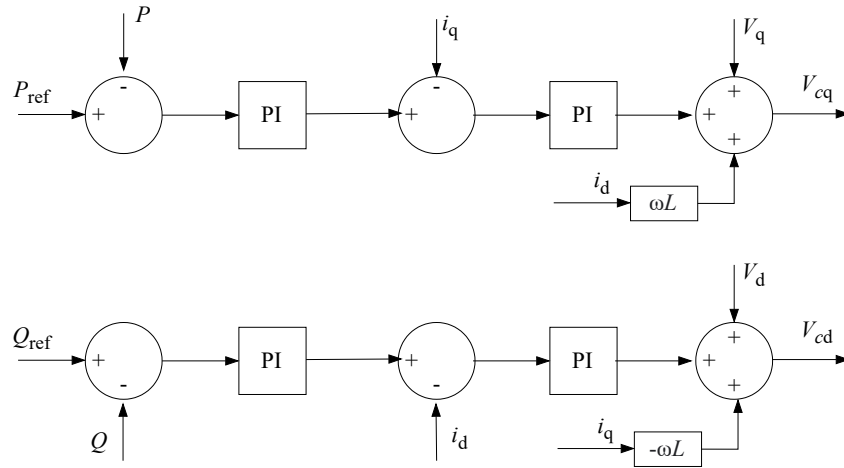


Figure 4.8: Decoupled control loops.

In Figure 4.8, P_{ref} and Q_{ref} are the active power reference and reactive power reference, which are set by the PPC.

4.4 Overall Layout and Control Structure of BESS

The overall structure of the BESS is shown in Figure 4.9. In here, components of BESS (e.g., battery, dc-dc converter, and VSC) and controllers (power plant controller (PPC) and converter controller) are discussed.

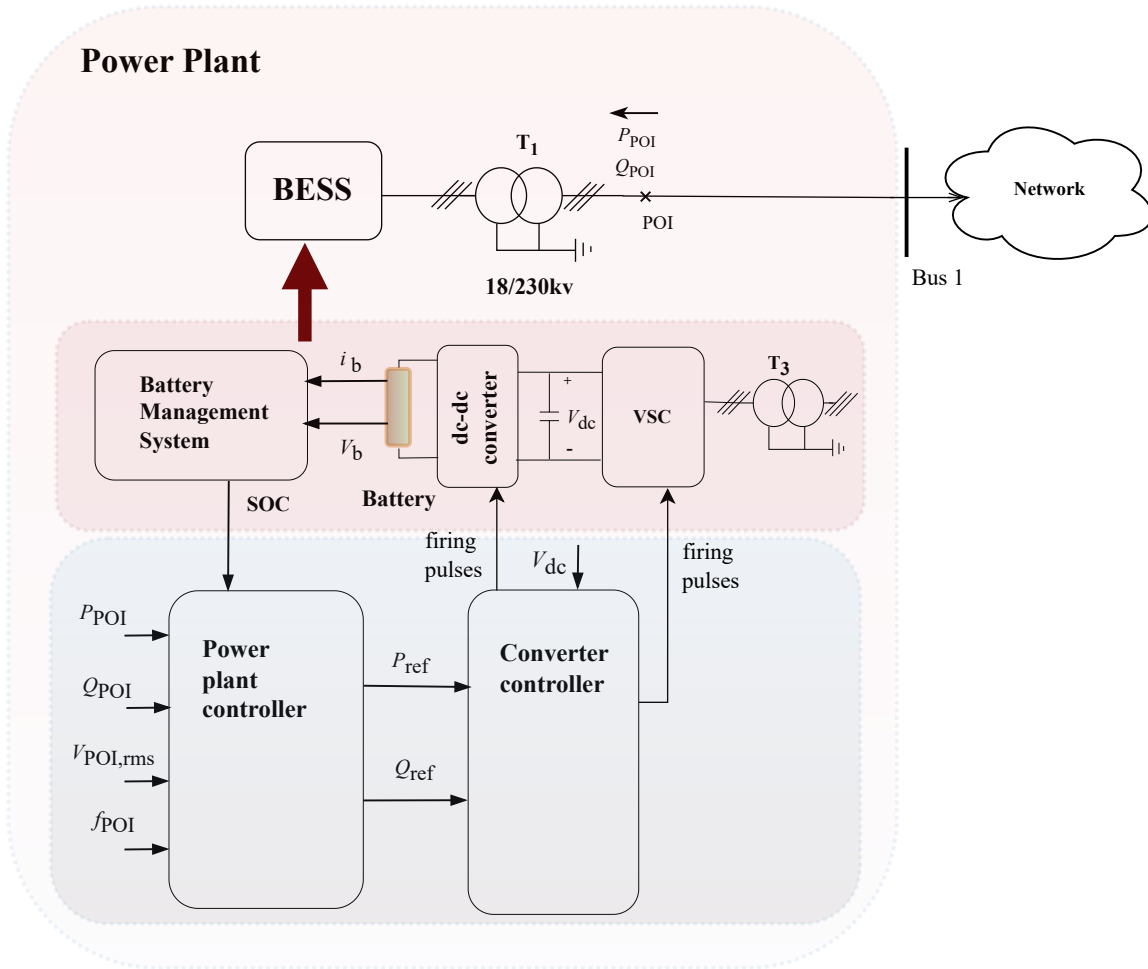


Figure 4.9: Block diagram of the BESS showing its components and controllers.

1. BESS

The BESS consists of a battery, dc-dc converter, VSC, and step-up transformer (T_3) along with a battery management system (BMS). SOC which is calculated by BMS is an input to the power plant controller. Battery current and terminal voltage are denoted by i_b and v_b , respectively.

2. Power plant controller (PPC)

As discussed in Chapter 3, the adaptive SOC-based droop controller is implemented in the PPC. The active power reference (P_{ref}) and reactive power reference (Q_{ref}) to the converter controller are generated by PPC. Corresponding power measurements (active power, P_{POI} , and reactive power, Q_{POI}) and frequency (f_{POI}) are measured at the point of interconnection; $V_{\text{POI,rms}}$ is the rms voltage at POI.

3. Converter controller

DC-link voltage regulation and generation of firing pulses for VSC to control the power exchange between the VSC and grid are implemented in the converter controller.

4.5 Synchronous Generator

In this study, the synchronous machine model in PACAD/EMTDC, shown in Figure 4.10, is employed. The inputs to the exciter model are the desired output field voltage (E_{fo}), the field current (I_{f}), terminal voltage (V_{T}), and current (I_{T}). The value of E_{ref0} is calculated to maintain steady-state operating conditions.

When the signal S2M switches state from 0 to 1, the electrical dynamics of the machine are released, and the rotor will be spinning at a constant speed. When LRR is switched from 0 to 1, mechanical dynamics will be released, and the governor and turbines will be initialized. W_{ref} is the reference speed (1 pu) to the governor and turbine and input to these models is the speed of the machine (w). Mechanical torque (T_{m}) is an input to the synchronous generator.

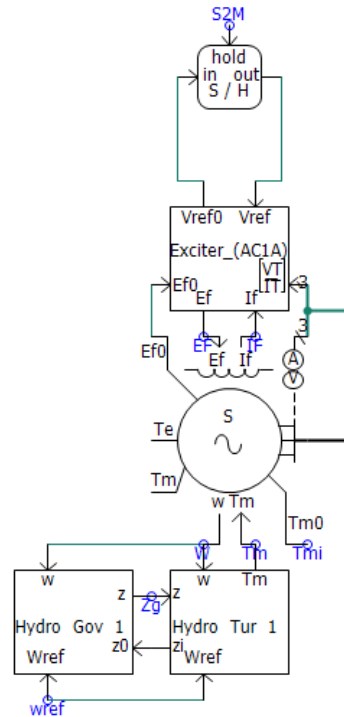


Figure 4.10: Synchronous machine model with exciter, governor, and turbine.

4.6 Wind Power Plant Model

In the simulations in this thesis, 160 MW of wind power generation consisting of 40 identical units of 4 MW, type-4 wind turbine generators is employed. Only one of the forty units is modeled and the scaling component in PSCAD/EMTDC is used to increase the power level of the unit to that of the equivalent wind farm.

As shown in Figure 4.11, the power plant controller generates the active power ($P_{w,ref}$) and reactive power ($Q_{w,ref}$) commands from the active power set-point ($P_{w,POI}$) and reactive power set-point ($Q_{w,POI}$) at POI.

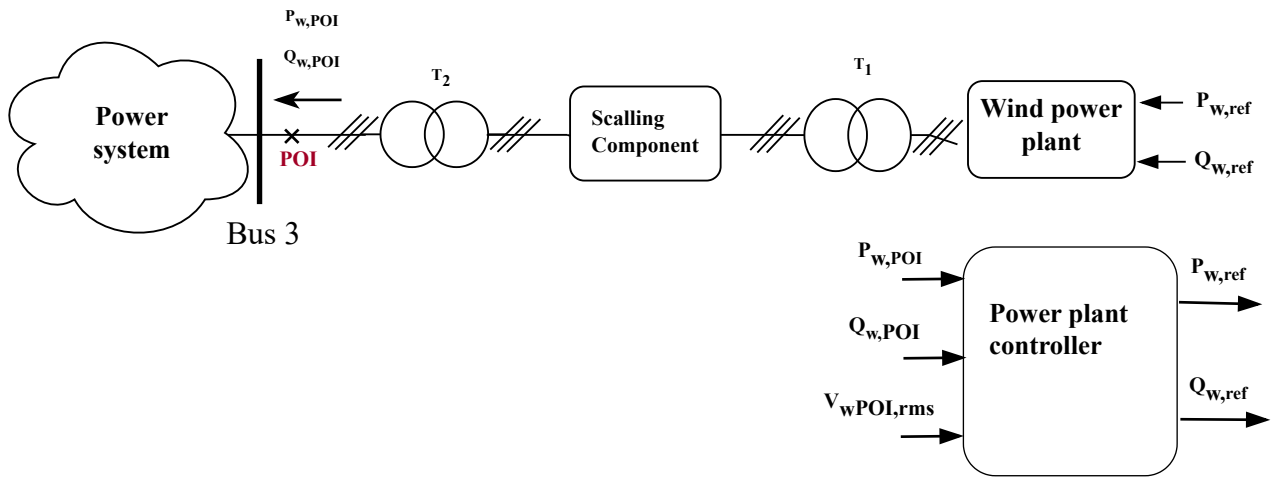


Figure 4.11: Wind power plant model.

4.7 Chapter summary

Non-linear Shepherd battery model, which is simple and accurate, is deployed as the battery model. The coulomb counting method is presented as the SOC calculation method. Detailed value model and average value model of bi-directional dc-dc converter are constructed. The proposed average value model has improved the simulation time considerably. The two-level VSC is employed to convert ac power to dc power and vice-versa. The synchronous machine model in PSCAD/EMTDC consisting of a governor, exciter, and turbine and wind power plant consisting of type 4 wind turbine is adopted for simulation studies.

Chapter 5

Detailed Assessment and Case Studies

In this chapter, simulation-based studies in PSCAD/EMTDC for performance evaluation of the proposed PFR method are presented. The following two test systems are employed:

1. A system consisting of a BESS, a load, and a synchronous generator (which is described in section 5.2), and

Objective: To observe the participation of heterogeneous batteries in PFR to distinct load changes in network.

2. The IEEE 9-bus system with a BESS, a wind power plant, and loads (which is described in section 5.3)

Objective: To observe the frequency at bus 4 for several disturbances in the system while heterogeneous batteries participate in PFR and to compare the effectiveness of the proposed PFR method with radical strategy and conservative strategy.

5.1 Summary of the Parameters of Models

In this section, the parameters of the BESS, synchronous generator (machine, governor, and exciter), and wind power plant employed for the above mentioned case studies are given (see Table 5.1). A comprehensive list of the parameters of each model is presented in the Appendix A.

It should be noted that the power capacity of BESS was selected based on the size of the test system and energy capacity was selected to observe a considerable variation of SOC during the simulation.

Table 5.1: Parameters of the Test System.

BESS		Capacity	50MW /5.152 MAh /10.76 MVAhr
		SOC_{\max}	0.9
		SOC_{\min}	0.1
		K_{\max}	0.505 (pu/Hz)
		Δf_{\max}	2 (Hz)
		Δf_{db}	0.02 (Hz)
Synchronous Generator	Machine	Machine model name	PSCAD standard machine model
		Capacity	900 MVA /200 MVA
		Inertia constant	4 s
	Governor	Governor /turbine model name	PSCAD standard Gov2/Tur1
		Proportional gain	0.1 pu
		Integral gain	0.033 pu
		Droop coefficient	0.2 pu
	Exciter	Model name	AC8B
		Proportional gain	10
		Integral gain	1.2
Derivative time constant		0.03 s	
Wind power plant		Capacity	160MW

5.2 Assessment of the Proposed PFR method

To observe the effectiveness of the proposed PFR method, the test system shown in Figure 5.1 is employed. The BESS is connected to bus 1 via a step-up transformer (T_1). A fixed load of 180 MW is connected to bus 2. A synchronous generator of 200 MVA is connected to bus 3. Two load-change scenarios at bus 1 are considered as mentioned below.

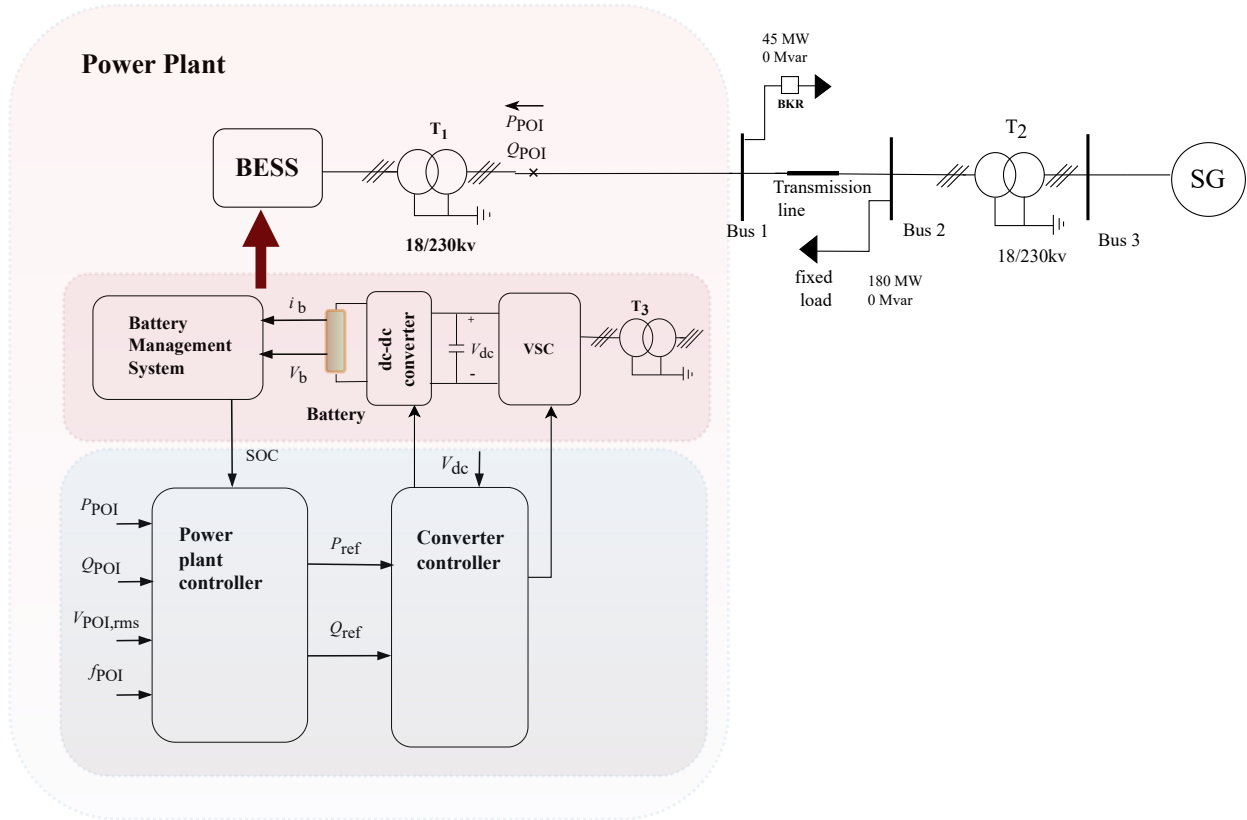


Figure 5.1: Schematic diagram of the test system.

A) Step load addition at bus 1

For addition of a 45 MW load at $t = 4.5$ s, grid frequency variations, BESS power, and synchronous generator power are observed with the initial SOC of the battery set

to 0.4 and 0.95. As shown in Figure 5.2(b), a battery with high SOC provides more power compared to a battery with low SOC. Also, steady state frequency deviation is improved by 72.36% by a battery with high SOC. As shown in Figure 5.2(c), since the BESS outputs more power when its SOC is high, the burden on the synchronous generator to participate in PFR is reduced. Additionally, Table 5.2 presents the steady state frequency deviation and maximum frequency dip for the two SOC values.

To investigate the influence of SOC on steady-state frequency deviation, for different SOC levels, steady-state frequency deviation is measured when a load of 15 MW is applied at bus 1 (see Figure 5.3). When SOC increases, steady state frequency deviation exponentially decays.

Table 5.2: Steady state frequency deviation and maximum frequency dip

SOC	Steady state frequency deviation (Hz)	Maximum frequency dip (Hz)
0.4	3.98	55.39
0.95	1.10	57.73

B) Step load shedding at bus 1

For a load tripping of 15 MW at $t = 4.5$ s grid frequency variations, BESS power, and synchronous generator power are observed when the battery SOC is 0.35 and 0.75. As shown in Figure 5.4, for a load tripping of 15 WM at bus 1, for the scenario where SOC is low (SOC is 0.35), the battery absorbs more power thus reducing maximum frequency rise.

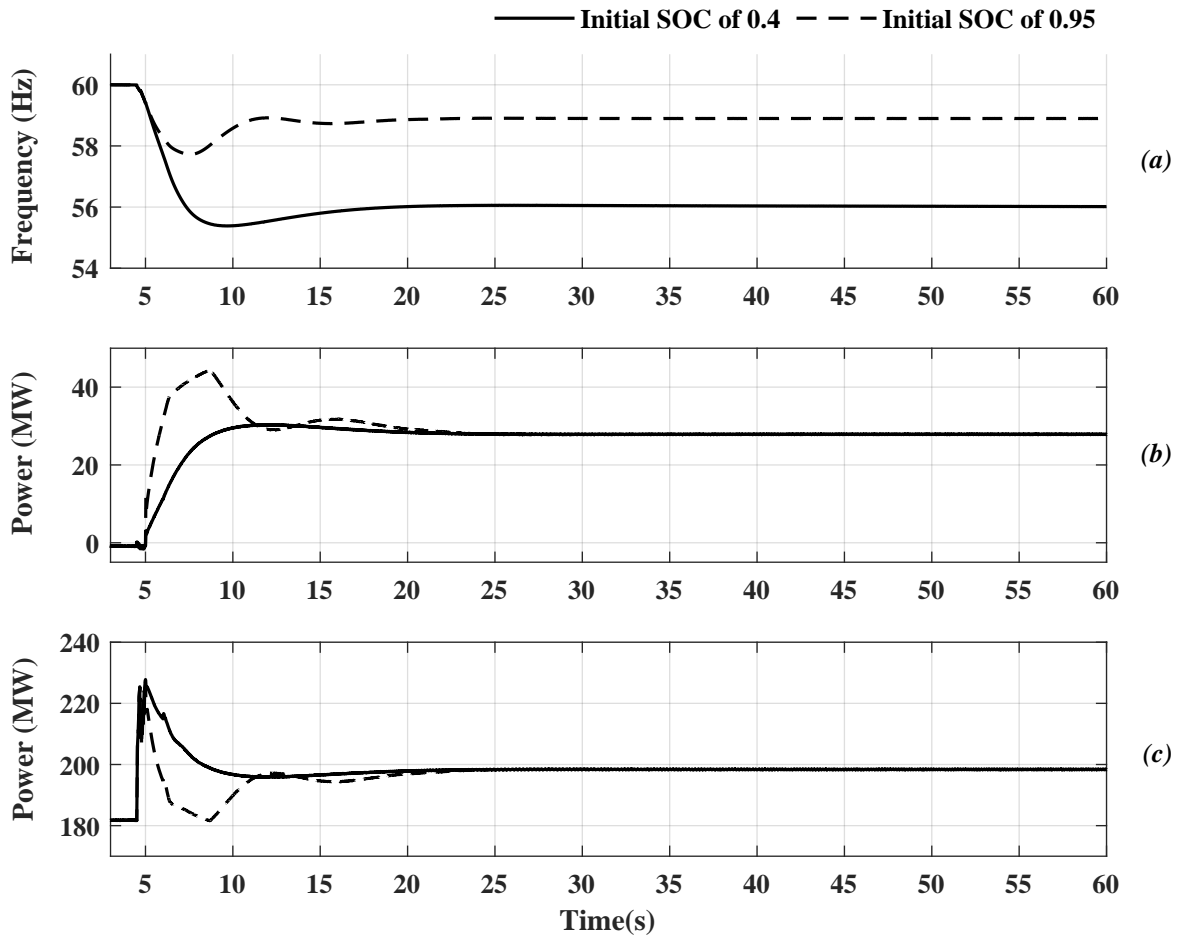


Figure 5.2: (a) Grid- frequency, (b) BESS power, (c) SG power for step load addition of 45 MW.

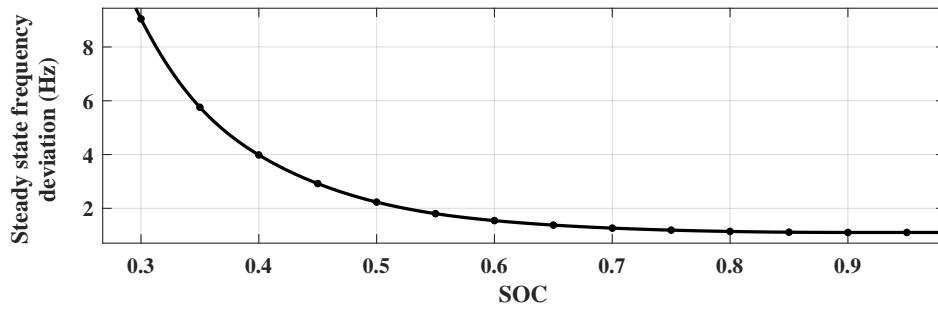


Figure 5.3: Steady state frequency deviation vs SOC for load addition of 15 MW.

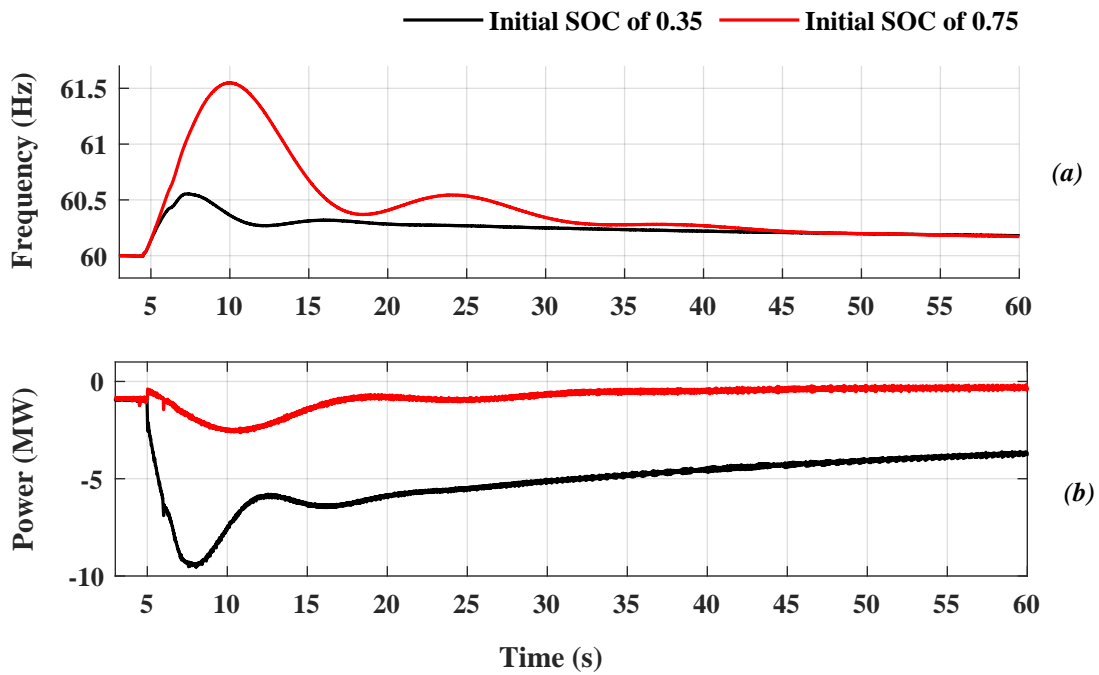


Figure 5.4: (a) Grid- frequency, (b) BESS power for step load reduction of 15 MW.

5.3 Case Studies with the IEEE 9-Bus System

The performance of the proposed control strategy is now evaluated using a modified version of the IEEE 9-bus test system with an installed BESS and a wind power plant for several scenarios. The schematic diagram of the simulation test system is shown Figure 5.5. The synchronous generator (G2) is modeled as a hydro-power plant with a capacity of 900 MVA. A BESS of 50 MW/5.152 MAh is connected to bus 4 via a step-up transformer. A wind power plant of 160 MW is connected to bus 9 via transformer T_3 . Three case studies are considered to comparatively evaluate the proposed adaptive droop control method with the fixed droop control method, conservative strategy, and radical strategy.

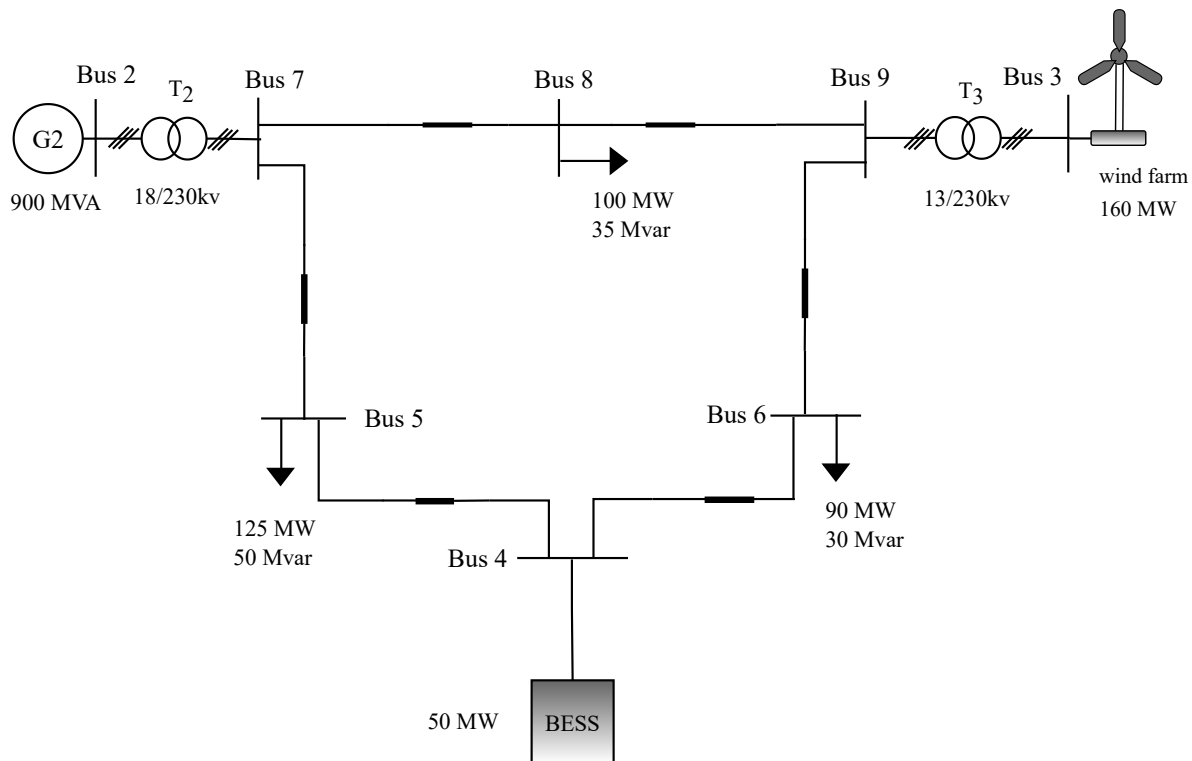


Figure 5.5: IEEE 9-bus system with installed BESS, wind power plant, and loads.

5.3.1 Case Study 1

For case study 1, four scenarios that are related to load change at bus 4 are considered (see Table 5.3). Figure 5.6 shows the frequency response at bus 4 for a load addition of 15 MW when PFR is provided by BESS with an initial SOC of 0.2 (Figure 5.6(a)) and 0.8 (Figure 5.6(b)), respectively.

Table 5.3: Case study 1

Step load disturbance	
Load tripping	Load addition
A step load reduction of 15 WM is applied at 10(s).	A step load addition of 15 WM is applied at 10(s).
For each disturbance, variation of grid-frequency is observed when battery initial	
(i) SOC is 0.2	
(ii) SOC is 0.8	

As compared with variable droop methods, for SOC of 0.2, the proposed method shows the lowest maximum frequency dip, while the fixed droop method and the proposed method exhibit similar frequency responses. When SOC is 0.8, the proposed method and radical method display similar frequency responses; compared with the fixed droop method maximum frequency dip has improved by 0.02 Hz.

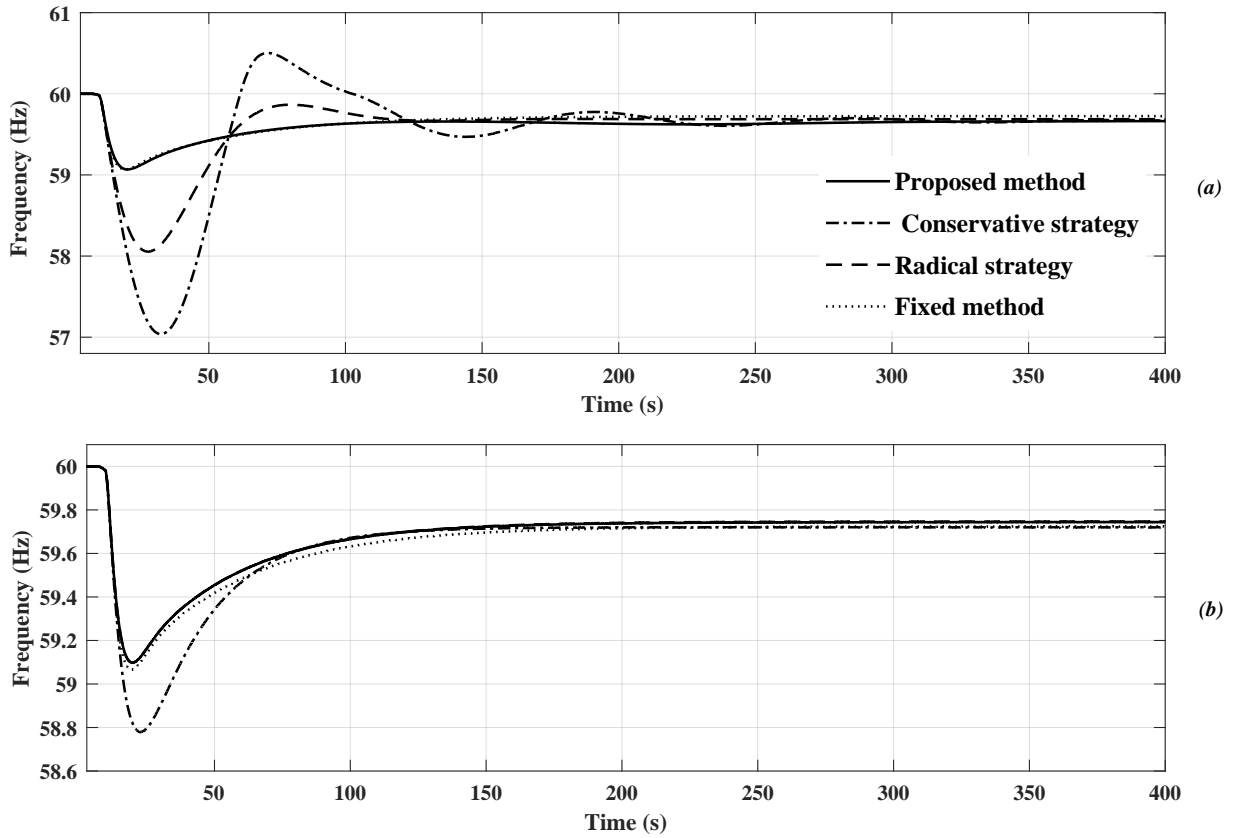


Figure 5.6: Response of frequency at bus 4 for load addition of 15 MW for (a) initial SOC of 0.2 (b) initial SOC of 0.8.

Table 5.4 shows the maximum frequency dip for each method for load addition of 15 MW.

Table 5.4: Comparison of maximum frequency dip for load addition of 15 MW

Method	Maximum frequency dip (Hz)	
	SOC 0.2	SOC 0.8
Proposed method	59.07	59.09
Conservative strategy	57.04	58.78
Radical strategy	58.06	59.09
Fixed method	59.07	59.07

Figure 5.7 shows the frequency response at bus 4 for a load tripping of 15 MW when PFR is provided by BESS with a SOC of 0.2 (Figure 5.7(a)) and 0.8 (5.7(b)), respectively. As compared with the variable droop methods, for both SOC values of 0.2 and 0.8, the proposed method shows the lowest maximum frequency rise; with the proposed the maximum frequency rise has improved by 0.046 Hz compared with the fixed droop method.

Table 5.5 shows the maximum frequency rise for each method for load tripping of 15 MW.

Table 5.5: Comparison of maximum frequency rise for load tripping of 15 MW

Method	Maximum frequency rise (Hz)	
	SOC 0.2	SOC 0.8
Proposed method	60.49	60.51
Conservative strategy	60.66	61.57
Radical strategy	60.49	61.05
Fixed method	60.53	60.53

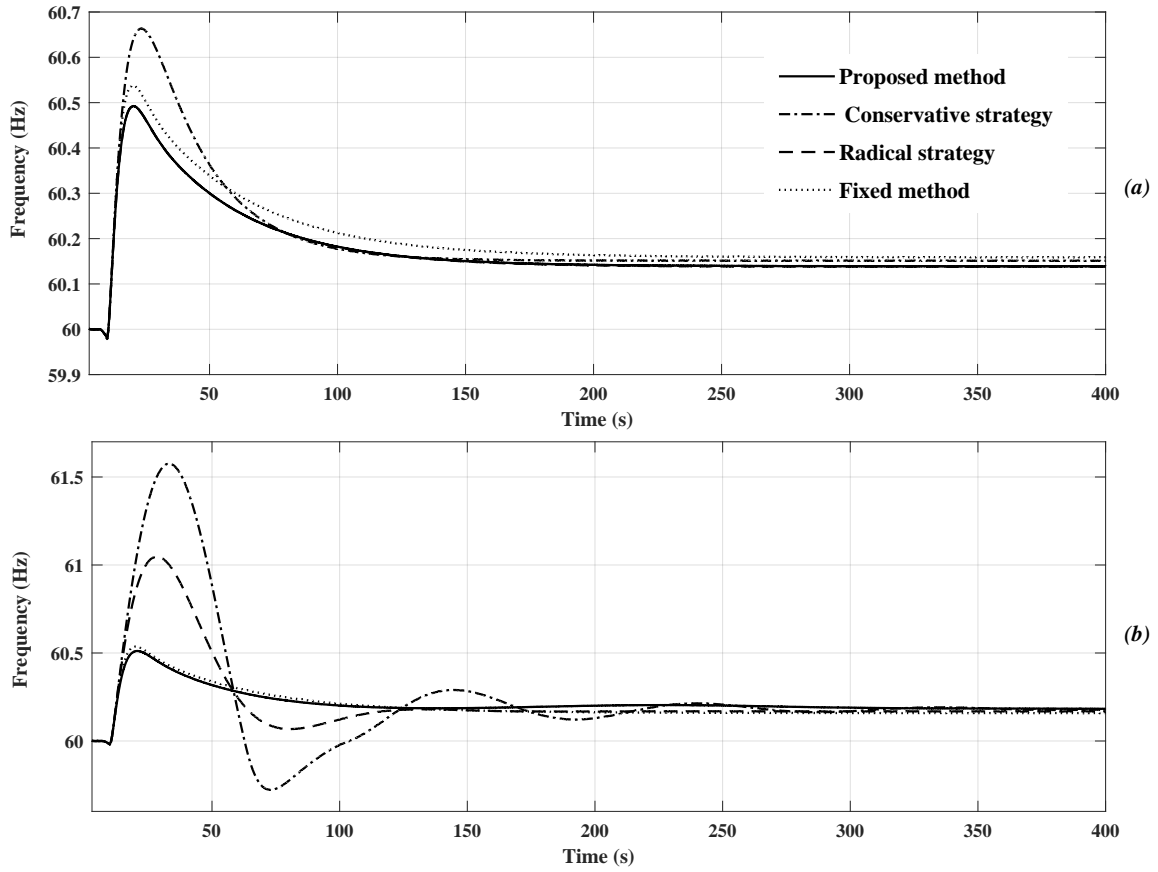


Figure 5.7: Response of frequency at bus 4 for load tripping of 15 MW for initial SOC of (a) 0.2 and (b) 0.8.

5.3.2 Case Study 2

In case study 2, four scenarios related to change of the output from the wind power plant are considered (see Table 5.6).

Table 5.6: Case study 2

Generation disturbance	
Loss of generation	Increase in generation
A 20% reduction of wind farm output is applied at 10(s).	A 20% increase of wind farm output is applied at 10(s).
For each disturbance, variation of grid-side parameters and battery-side are observed when battery initial (i) SOC is 0.2 (ii) SOC is 0.8	

Figure 5.8 shows the frequency response at bus 4 for a 20% increase in the wind power plant's output when PFR is provided by BESS with an initial SOC of 0.2 (Figure 5.8(a)) and 0.8 (Figure 5.8(b)), respectively. For SOC of 0.2, the variable droop method, radical method, and fixed droop method show similar frequency responses and the conservative strategy method displays the highest frequency rise. For SOC of 0.8, the proposed method and the fixed droop method show the lowest maximum frequency rise. The proposed method and the fixed droop method show similar frequency responses. Table 5.7 shows the maximum frequency rise for each method for a generation increase of 20%.

Figure 5.9 shows the frequency response at bus 4 for a 20% reduction of wind power plant's output when PFR is provided by BESS with an initial SOC of 0.2 (Figure 5.9(a)) and 0.8 (Figure 5.9(b)), respectively. For SOC of 0.2, the proposed method and fixed droop method have the lowest maximum frequency dip and the conservative method shows the highest maximum frequency dip. For SOC of 0.8, the proposed method and the radical

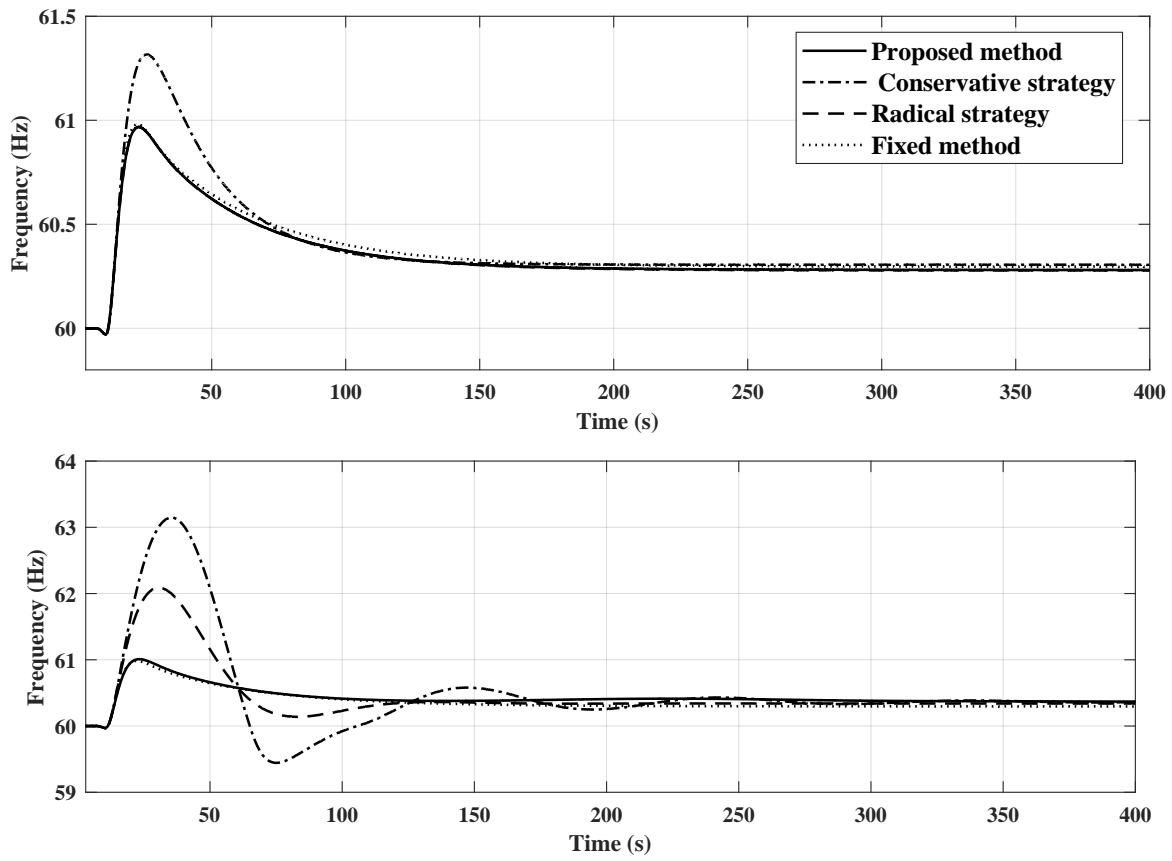


Figure 5.8: Response of frequency at bus 4 for generation increase of 20% for an initial SOC of (a) 0.2 and (b) 0.8.

method display the lowest maximum frequency dip. Table 5.8 shows the maximum frequency dip for each method for wind generation reduction of 20%.

Table 5.7: Comparison of maximum frequency rise for wind generation increase

Method	Maximum frequency rise (Hz)	
	SOC 0.2	SOC 0.8
Proposed method	60.96	61.01
Conservative strategy	61.31	63.14
Radical strategy	60.96	62.08
Fixed method	60.98	61.01

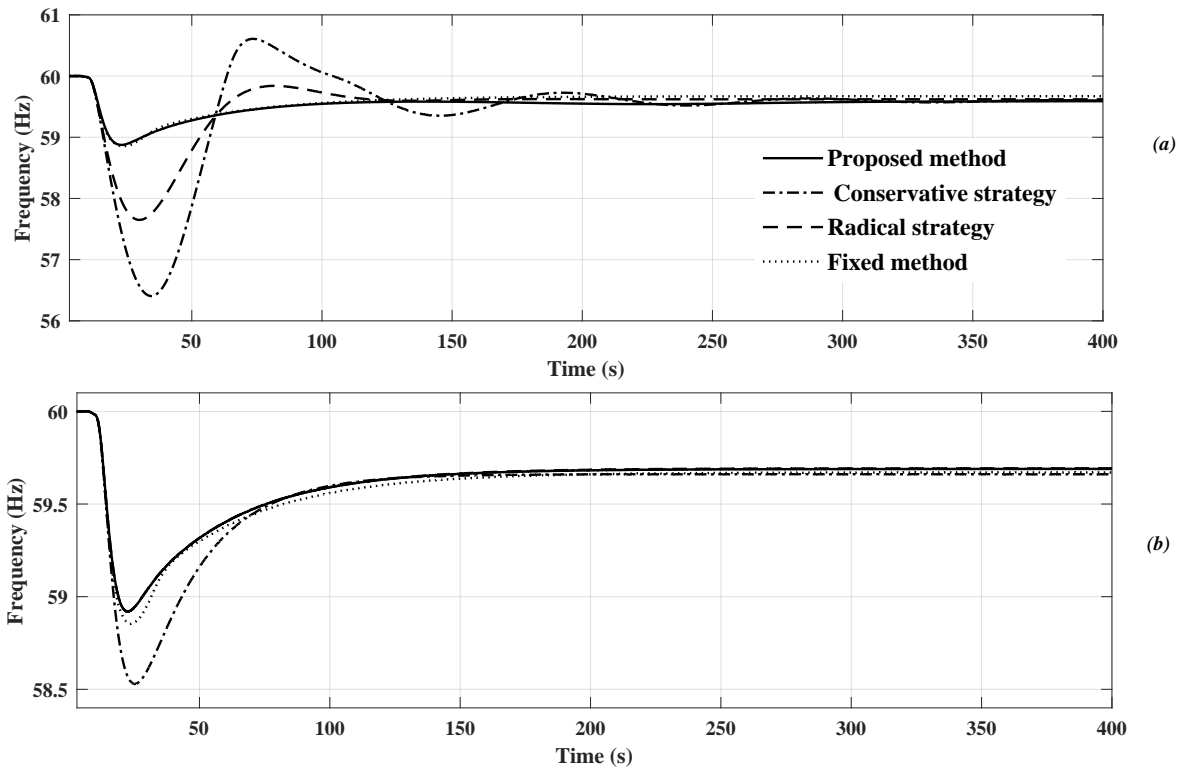


Figure 5.9: Response of frequency at bus 4 for generation reduction of 20% for (a) initial SOC of 0.2 (b) initial SOC of 0.8.

Table 5.8: Comparison of maximum frequency dip for wind generation reduction

Method	Maximum frequency dip (Hz)	
	SOC 0.2	SOC 0.8
Proposed method	58.85	58.92
Conservative strategy	56.41	58.52
Radical strategy	57.65	58.92
Fixed method	58.85	58.85

From the above simulation results, the following observations may be drawn.

- Among the considered droop strategies, the proposed method shows improved frequency response in terms of maximum frequency dip/maximum frequency rise irrespective of the SOC of the battery. Even when a frequency contingency event occurs in which the battery is required to discharge when its SOC is low, the BESS responds properly without affecting the grid frequency. Also for a scenario where the battery is required to charge, even though its SOC is high, the battery will charge and support the system.
- Conservative strategy shows the highest maximum dip/maximum rise among all methods irrespective of the SOC.
- Radical strategy demonstrates better performance when BESS is requested to discharge when its SOC is high and BESS is requested to charge when its SOC is low. However, when the BESS ought to discharge with a low SOC (or charge with a high SOC), it does not show an improved frequency response.

5.3.3 Case Study 3

In case study 3, a special scenario that shows the frequency response for a load addition, while BESS providing PFR with and without the enhancement of short-term frequency support, is considered. The objective is to exhibit how BESS with enhanced short-term frequency support improves the frequency response in terms of reduction in maximum frequency dip.

As mentioned in Chapter 3, section 3.2.3, one limitation of the proposed method is only when the SOC is greater than SOC_{\max} , it gives maximum power to the system. From the grid's point of view, it is a disadvantage, as even with a relatively low SOC, large-scale BESS can participate in PFR for an appropriate time at maximum droop coefficient (K_{\max}). In the same manner, a relatively high SOC battery can be charged at K_{\max} for a certain time. Therefore, droop coefficients (K_d and K_c) are modified to $K_{d,\text{mod}}$ and $K_{c,\text{mod}}$ to give dynamic support, which in return reduces the maximum frequency dip/rise.

Case study 3 is presented to show the advantage of the utilization of low SOC BESS with modified discharge droop coefficient ($K_{d,\text{mod}}$) for PFR service. Hence, the response of the grid frequency to a load addition of 15 MW at bus 4 with a BESS with a SOC of 0.2 providing PFR is considered. Two scenarios as described below are employed (see Figure 5.10).

1. BESS with K_d : Throughout the simulation, BESS is discharged at K_d .
2. BESS with $K_{d,\text{mod}}$: Initially, discharging droop coefficient is set to K_{\max} and brought back to K_d within a period of 300 s.

It must be noted that since a 50 MW battery has a very high energy capacity (10.76 MVAhr), T_{boost} appears to be a larger value; therefore for the simplicity of simulation T_{boost} is considered as 300 s. The calculation of T_{boost} is presented in (3.5). As shown in Figure 5.11(a),

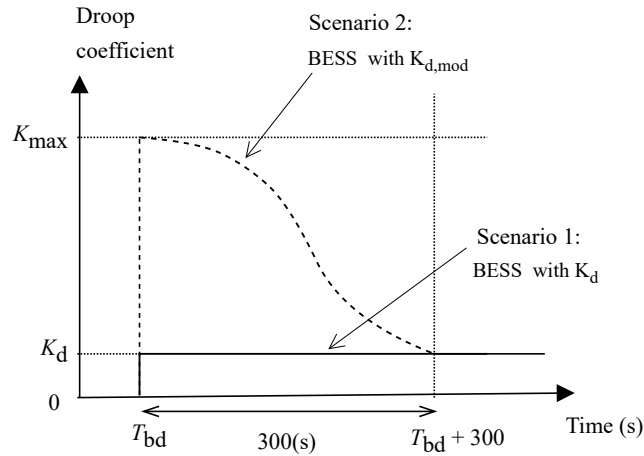


Figure 5.10: Variations of K_d and $K_{d,mod}$ with time.

by modifying K_d to $K_{d,mod}$, the maximum frequency dip can be improved by 1.32 Hz. Also Figure 5.11(b) shows the variation of SOC with each scenario. At $t = 300$ s, the SOC of BESS with K_d is 0.1958 and for BESS with $K_{d,mod}$ the SOC is 0.1945. The deviation of the SOC from initial SOC (0.2) for each is mentioned in Table 5.9.

Table 5.9: Deviation of SOC

	BESS with K_d	BESS with $K_{d,mod}$
Deviation of SOC	0.0048	0.0055

It is evident that the deviation of the SOC from the initial SOC is also significantly low for BESS with $K_{d,mod}$. Therefore, BESS being discharged at K_{max} , for a relatively short period of time (300 s) does not negatively impact SOC. Additionally, the way K_d and $K_{d,mod}$ vary for different SOC levels (SOC of 0.2, 0.45, 0.85, and 1.0) is shown in Figure 5.12. For each SOC level, the value of the discharging droop coefficient starts with K_{max} and is brought

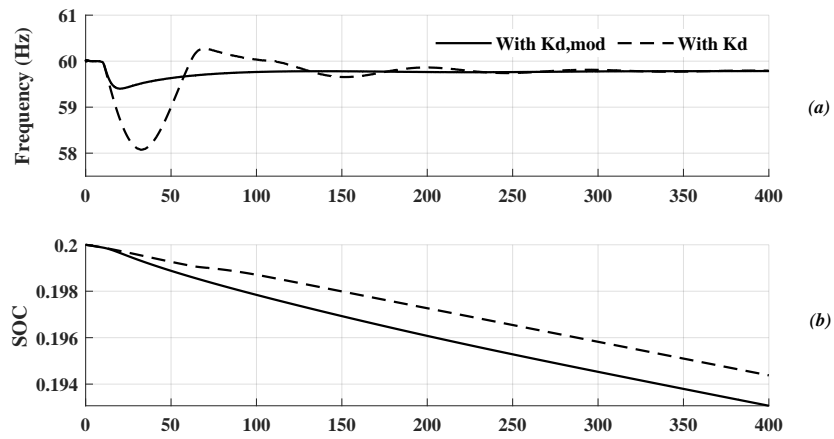


Figure 5.11: (a) Frequency response at bus 4 for load addition of 15 MW (b) battery SOC

back to K_d within 300 s.

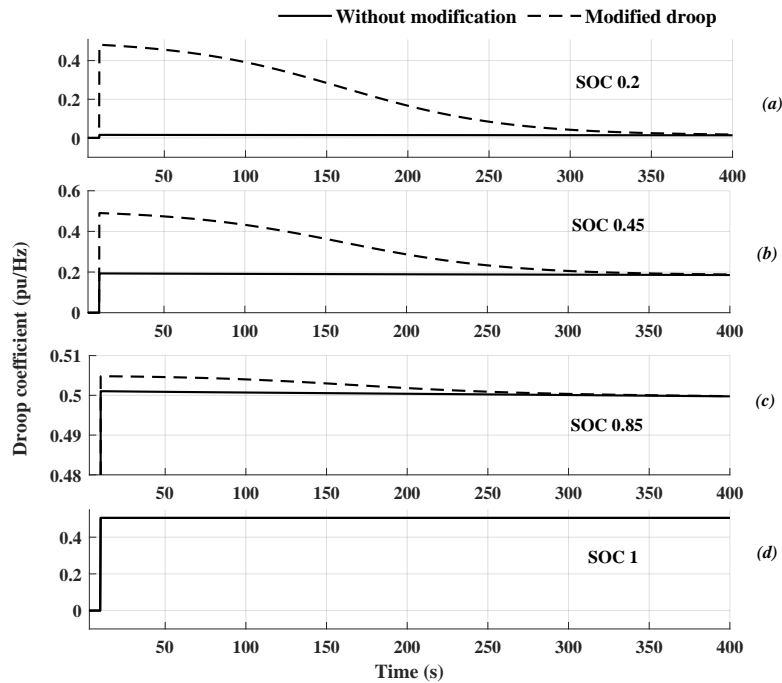


Figure 5.12: Variations of K_d and $K_{d,mod}$ for a load change of 15 MW.

5.4 Chapter Summary

The behavior of a BESS participating in PFR with distinct SOC levels according to the proposed method was observed. The results indicated that during an under-frequency event, a battery with high SOC gives more power reducing the maximum frequency dip as expected, and during an over-frequency event, a battery with low SOC absorbs more power reducing the maximum frequency rise as predicted. The effectiveness of the proposed method was compared with the conservative method and radical method while the test system was exposed to multiple contingencies. The proposed method showed an improved frequency response in terms of maximum frequency dip/maximum frequency rise irrespective of the SOC of the battery. Furthermore, it showed that the variation of battery SOC, which can happen due to the additional boost given to the droop coefficients, is considerably low. Therefore, it can be stated that because of the proposed method, battery capacity can be preserved to support the grid with future contingencies. Additionally, due to the utilization of the proposed method, a low SOC battery can support the grid for an under-frequency event or a high SOC battery can support during an over-frequency event for a considerably longer time period.

Chapter 6

Contributions, Conclusions, and Recommendation for future work

6.1 Contributions and Conclusions

The main contribution of this thesis is the development of an improved adaptive SOC-based droop control for BESS participating in PFR. The contributions made throughout the research along with conclusions drawn and future directions to be pursued are described below.

1. Comprehensive review of different PFR techniques and their drawbacks, different PFR techniques of BESS proposed in the literature along with their limitations, and finally dynamic models of battery for frequency regulation.

Several PFR control strategies are proposed in the literature to improve the frequency response of power systems with a high penetration of renewable energy resources. Since the droop control method shows sufficient accuracy and simplicity,

the variable droop control algorithm, which takes into account the influence of SOC on the droop coefficient, is often utilized in PFR studies. Hence, the development of an adaptive SOC-based PFR method that demonstrates proper balance between providing PFR and maintaining SOC is an important task for future power grids with high penetration of renewable energy generation,

2. Development of an improved adaptive PFR control strategy for BESS considering SOC of each battery.

The proposed adaptive SOC-based control strategy allows batteries with low SOC to charge more (during over-frequency event) and discharge less (during under-frequency event) and batteries with high SOC to charge less (during over-frequency event) and discharge more (during under-frequency event). It also prevents frequent charge/discharge of batteries. It also enhances short-term frequency response by giving an additional boost to the droop to reduce maximum frequency dip/rise.

3. Modelling of BESSs including a dynamic model of battery, bi-directional dc-dc converter (detailed model and average-value model), and VSC along with corresponding controllers.

It can be concluded that the non-linear Shepherd battery model is simple and accurate for frequency regulation studies provided that the representation of the fast dynamics process of batteries is not required. The detailed modeling of many batteries with dedicated bi-directional dc-dc converters will reduce the simulation speed considerably. More importantly, the replacement of detailed switching models with average-value models does not negatively impact grid-side parameters and battery-side parameters and shows good accuracy even during the transient period.

4. Integrating the developed BESS model along with the proposed control strategy into the PSCAD/EMTDC simulator.

First, the BESS with two distinct SOC levels was added separately to a test system with a synchronous generator and fixed load, and variation of grid-side parameters and battery-side parameters were observed while the system undergoing load change events. Then the BESS model was successfully integrated into a larger system (the IEEE 9-bus system).

5. Observe the performance of the proposed control strategy under several types of disturbance incorporating the model into small to large-scale test systems.

The proposed adaptive SOC-based control strategy showed improved frequency response in terms of maximum frequency dip/maximum frequency rise compared to three existing methods in the literature.

6.2 Recommendation for Future Work

1. Integration of the enhanced-capacity BESS to a much larger system with an increased level of renewable energy generations to observe the performance evaluation of the proposed method.
2. Development of an optimal sizing and allocation method for BESS considering both technical and economical constraints.

References

- [1] U. Akram, M. Nadarajah, R. Shah, and F. Milano, “A review on rapid responsive energy storage technologies for frequency regulation in modern power systems,” *Renewable and Sustainable Energy Reviews*, vol. 120, p. 109626, 2020. [Online]. Available: <https://www.sciencedirect.com/science/article/pii/S1364032119308330>
- [2] H. Gu, R. Yan, and T. Saha, “Review of system strength and inertia requirements for the national electricity market of australia,” *CSEE Journal of Power and Energy Systems*, vol. 5, no. 3, pp. 295–305, 2019.
- [3] Z. Wu, W. Gao, T. Gao, W. Yan, H. Zhang, S. Yan, and X. Wang, “State-of-the-art review on frequency response of wind power plants in power systems,” *Journal of Modern Power Systems and Clean Energy*, vol. 6, no. 1, pp. 1–16, 2018.
- [4] K. V. Vidyanandan and N. Senroy, “Primary frequency regulation by deloaded wind turbines using variable droop,” *IEEE Transactions on Power Systems*, vol. 28, no. 2, pp. 837–846, 2013.
- [5] R. Rajan, F. M. Fernandez, and Y. Yang, “Primary frequency control techniques for large-scale pv-integrated power systems: A review,” *Renewable and Sustainable Energy Reviews*, vol. 144, p. 110998, 2021. [Online]. Available: <https://www.sciencedirect.com/science/article/pii/S1364032121002884>
- [6] P. Zarina, S. Mishra, and P. Sekhar, “Exploring frequency control capability of a pv system in a hybrid pv-rotating machine-without storage system,” *International Journal of Electrical Power and Energy Systems*, vol. 60, no. Complete, pp. 258–267, 2014.
- [7] A. F. Hoke, M. Shirazi, S. Chakraborty, E. Muljadi, and D. Maksimovic, “Rapid active power control of photovoltaic systems for grid frequency support,” *IEEE Journal of Emerging and Selected Topics in Power Electronics*, vol. 5, no. 3, pp. 1154–1163, 2017.
- [8] J. W. Shim, G. Verbič, N. Zhang, and K. Hur, “Harmonious integration of faster-acting energy storage systems into frequency control reserves in power grid with high renewable generation,” *IEEE Transactions on Power Systems*, vol. 33, no. 6, pp. 6193–6205, 2018.

-
- [9] D.-I. Stroe, V. Knap, M. Swierczynski, A.-I. Stroe, and R. Teodorescu, "Operation of a grid-connected lithium-ion battery energy storage system for primary frequency regulation: A battery lifetime perspective," *IEEE Transactions on Industry Applications*, vol. 53, no. 1, pp. 430–438, 2017.
- [10] D. Zhu and Y.-J. A. Zhang, "Optimal coordinated control of multiple battery energy storage systems for primary frequency regulation," *IEEE Transactions on Power Systems*, vol. 34, no. 1, pp. 555–565, 2019.
- [11] A.M.S.M.H.S.Attanayaka, J.P.Karunadasa, and K.T.M.U.Hemapala, "Estimation of state of charge for lithium-ion batteries - a review," *AIMS Energy*, vol. 7, no. 2, pp. 186–210, 2019. [Online]. Available: <https://www.aimspress.com/article/doi/10.3934/energy.2019.2.186>
- [12] A. Turk, M. Sandelic, G. Noto, J. R. Pillai, and S. K. Chaudhary, "Primary frequency regulation supported by battery storage systems in power system dominated by renewable energy sources," *The Journal of Engineering*, vol. 2019, no. 18, pp. 4986–4990, 2019. [Online]. Available: <https://ietresearch.onlinelibrary.wiley.com/doi/abs/10.1049/joe.2018.9349>
- [13] P. Kundur and N. Balu, *Power System Stability and Control*, ser. EPRI power system engineering series. McGraw-Hill, 1994. [Online]. Available: <https://books.google.ca/books?id=0fPGngEACAAJ>
- [14] "Grid-scale battery storage frequently asked questions." [Online]. Available: <https://www.nrel.gov/docs/fy19osti/74426.pdf>
- [15] K. Divya and J. Østergaard, "Battery energy storage technology for power systems—an overview," *Electric Power Systems Research*, vol. 79, no. 4, pp. 511–520, 2009. [Online]. Available: <https://www.sciencedirect.com/science/article/pii/S0378779608002642>
- [16] A. Oudalov, D. Chartouni, and C. Ohler, "Optimizing a battery energy storage system for primary frequency control," *IEEE Transactions on Power Systems*, vol. 22, no. 3, pp. 1259–1266, 2007.
- [17] T. Borsche, A. Ulbig, M. Koller, and G. Andersson, "Power and energy capacity requirements of storages providing frequency control reserves," in *2013 IEEE Power Energy Society General Meeting*, 2013, pp. 1–5.
- [18] P. Mercier, R. Cherkaoui, and A. Oudalov, "Optimizing a battery energy storage system for frequency control application in an isolated power system," *IEEE Transactions on Power Systems*, vol. 24, no. 3, pp. 1469–1477, 2009.
-

-
- [19] S. Bradbury, J. Hayling, P. Papadopoulos, and N. Heyward, “Smarter network storage electricity storage in gb: Sns 4.7 recommendations for regulatory and legal framework (sdrc 9.5),” 2015.
- [20] “Ds3: Frequency control workstream 2015, eirgrid and soni, dublin, ireland,” 2015.
- [21] J. Seasholtz, “Grid-scale energy storage demonstration of ancillary services using the ultrabattery technology.” [Online]. Available: <https://www.osti.gov/biblio/1349503>
- [22] Z. Tan, X. Li, L. He, Y. Li, and J. Huang, “Primary frequency control with bess considering adaptive soc recovery,” *International Journal of Electrical Power Energy Systems*, vol. 117, p. 105588, 2020. [Online]. Available: <https://www.sciencedirect.com/science/article/pii/S0142061519313845>
- [23] N. Nguyen, D. Pandit, R. Quigley, and J. Mitra, “Frequency response in the presence of renewable generation: Challenges and opportunities,” *IEEE Open Access Journal of Power and Energy*, vol. 8, pp. 543–556, 2021.
- [24] L. Meng, J. Zafar, S. K. Khadem, A. Collinson, K. C. Murchie, F. Coffele, and G. M. Burt, “Fast frequency response from energy storage systems—a review of grid standards, projects and technical issues,” *IEEE Transactions on Smart Grid*, vol. 11, no. 2, pp. 1566–1581, 2020.
- [25] Y. Cheng, R. Azizipناه-Abarghoee, S. Azizi, L. Ding, and V. Terzija, “Smart frequency control in low inertia energy systems based on frequency response techniques: A review,” *Applied Energy*, vol. 279, p. 115798, 2020. [Online]. Available: <https://www.sciencedirect.com/science/article/pii/S0306261920312800>
- [26] L. Radaelli and S. Martinez, “Frequency stability analysis of a low inertia power system with interactions among power electronics interfaced generators with frequency response capabilities,” *Applied Sciences*, vol. 12, no. 21, 2022. [Online]. Available: <https://www.mdpi.com/2076-3417/12/21/11126>
- [27] F. Arrigo, E. Bompard, M. Merlo, and F. Milano, “Assessment of primary frequency control through battery energy storage systems,” *International Journal of Electrical Power Energy Systems*, vol. 115, p. 105428, 2020. [Online]. Available: <https://www.sciencedirect.com/science/article/pii/S0142061519307598>
- [28] A. M. Shotorbani, B. Mohammadi-Ivatloo, L. Wang, S. Ghassem-Zadeh, and S. H. Hosseini, “Distributed secondary control of battery energy storage systems in a stand-alone microgrid,” *IET Generation, Transmission & Distribution*, vol. 12, no. 17, pp. 3944–3953, 2018. [Online]. Available: <https://ietresearch.onlinelibrary.wiley.com/doi/abs/10.1049/iet-gtd.2018.0105>
-

-
- [29] N. Vazquez, S. S. Yu, T. K. Chau, T. Fernando, and H. H.-C. Iu, "A fully decentralized adaptive droop optimization strategy for power loss minimization in microgrids with pv-bess," *IEEE Transactions on Energy Conversion*, vol. 34, no. 1, pp. 385–395, 2019.
- [30] A. Attya, J. Dominguez-Garcia, and O. Anaya-Lara, "A review on frequency support provision by wind power plants: Current and future challenges," *Renewable and Sustainable Energy Reviews*, vol. 81, pp. 2071–2087, 2018. [Online]. Available: <https://www.sciencedirect.com/science/article/pii/S1364032117309553>
- [31] I. A. Hiskens, "Dynamics of type-3 wind turbine generator models," *IEEE Transactions on Power Systems*, vol. 27, no. 1, pp. 465–474, 2012.
- [32] G. C. Tarnowski, P. C. Kjar, P. E. Sorensen, and J. Ostergaard, "Variable speed wind turbines capability for temporary over-production," in *2009 IEEE Power Energy Society General Meeting*, 2009, pp. 1–7.
- [33] I. A. Gowaid, A. El-Zawawi, and M. El-Gammal, "Improved inertia and frequency support from grid-connected dfig wind farms," in *2011 IEEE/PES Power Systems Conference and Exposition*, 2011, pp. 1–9.
- [34] E. Ela, V. Gevorgian, P. Fleming, Y. C. Zhang, M. Singh, E. Muljadi, A. Scholbrook, J. Aho, A. Buckspan, L. Pao, V. Singhvi, A. Tuohy, P. Pourbeik, D. Brooks, and N. Bhatt, "Active power controls from wind power: Bridging the gaps." [Online]. Available: <https://www.osti.gov/biblio/1117060>
- [35] A. Buckspan, J. Aho, P. Fleming, Y. Jeong, and L. Pao, "Combining droop curve concepts with control systems for wind turbine active power control," in *2012 IEEE Power Electronics and Machines in Wind Applications*, 2012, pp. 1–8.
- [36] J. Aho, A. Buckspan, J. Laks, P. Fleming, Y. Jeong, F. Dunne, M. Churchfield, L. Pao, and K. Johnson, "A tutorial of wind turbine control for supporting grid frequency through active power control," in *2012 American Control Conference (ACC)*, 2012, pp. 3120–3131.
- [37] M. A. Pinazo, R. A. Arias, and J. M. Tarrillo, "Comparison of primary frequency control methods for wind turbines based on the doubly fed induction generator," *Wind Engineering*, vol. 46, no. 6, pp. 1923–1947, 2022. [Online]. Available: <https://doi.org/10.1177/0309524X221114350>
- [38] A. Hoke and D. Maksimović, "Active power control of photovoltaic power systems," in *2013 1st IEEE Conference on Technologies for Sustainability (SusTech)*, 2013, pp. 70–77.
-

-
- [39] B.-I. Crăciun, T. Kerekes, D. Séra, and R. Teodorescu, “Frequency support functions in large pv power plants with active power reserves,” *IEEE Journal of Emerging and Selected Topics in Power Electronics*, vol. 2, no. 4, pp. 849–858, 2014.
- [40] A. Sangwongwanich, Y. Yang, F. Blaabjerg, and D. Sera, “Delta power control strategy for multistring grid-connected pv inverters,” *IEEE Transactions on Industry Applications*, vol. 53, no. 4, pp. 3862–3870, 2017.
- [41] X. Lyu, Z. Xu, and J. Zhao, “A coordinated frequency control strategy for photovoltaic system in microgrid,” *Journal of International Council on Electrical Engineering*, vol. 8, no. 1, pp. 37–43, 2018. [Online]. Available: <https://doi.org/10.1080/22348972.2018.1470295>
- [42] G. Yan, S. Liang, Q. Jia, and Y. Cai, “Novel adapted de-loading control strategy for pv generation participating in grid frequency regulation,” *The Journal of Engineering*, vol. 2019, no. 16, pp. 3383–3387, 2019. [Online]. Available: <https://ietresearch.onlinelibrary.wiley.com/doi/abs/10.1049/joe.2018.8481>
- [43] X. Luo, J. Wang, M. Dooner, and J. Clarke, “Overview of current development in electrical energy storage technologies and the application potential in power system operation,” *Applied Energy*, vol. 137, pp. 511–536, 2015. [Online]. Available: <https://www.sciencedirect.com/science/article/pii/S0306261914010290>
- [44] J. Arseneaux, “20 mw flywheel frequency regulation plant.” [Online]. Available: <https://www.osti.gov/biblio/1351296>
- [45] K. Sahay and B. Dwivedi, “Supercapacitors energy storage system for power quality improvement: An overview,” *Journal of Electrical Systems*, vol. 5, 12 2009.
- [46] H. Chen, T. N. Cong, W. Yang, C. Tan, Y. Li, and Y. Ding, “Progress in electrical energy storage system: A critical review,” *Progress in Natural Science*, vol. 19, no. 3, pp. 291–312, 2009. [Online]. Available: <https://www.sciencedirect.com/science/article/pii/S100200710800381X>
- [47] M. D. Mufti, S. J. Iqbal, S. A. Lone, and Q.-u. Ain, “Supervisory adaptive predictive control scheme for supercapacitor energy storage system,” *IEEE Systems Journal*, vol. 9, no. 3, pp. 1020–1030, 2015.
- [48] S. C. Smith, P. Sen, and B. Kroposki, “Advancement of energy storage devices and applications in electrical power system,” in *2008 IEEE Power and Energy Society General Meeting - Conversion and Delivery of Electrical Energy in the 21st Century*, 2008, pp. 1–8.
-

-
- [49] S. Mousavi G, F. Faraji, A. Majazi, and K. Al-Haddad, “A comprehensive review of flywheel energy storage system technology,” *Renewable and Sustainable Energy Reviews*, vol. 67, pp. 477–490, 2017. [Online]. Available: <https://www.sciencedirect.com/science/article/pii/S1364032116305597>
- [50] F. Díaz-González, M. Hau, A. Sumper, and O. Gomis-Bellmunt, “Coordinated operation of wind turbines and flywheel storage for primary frequency control support,” *International Journal of Electrical Power Energy Systems*, vol. 68, pp. 313–326, 2015. [Online]. Available: <https://www.sciencedirect.com/science/article/pii/S0142061514007893>
- [51] S. A. P. Kani, P. Wild, and T. K. Saha, “Improving predictability of renewable generation through optimal battery sizing,” *IEEE Transactions on Sustainable Energy*, vol. 11, no. 1, pp. 37–47, 2020.
- [52] M. Farhadi and O. Mohammed, “Energy storage technologies for high-power applications,” *IEEE Transactions on Industry Applications*, vol. 52, no. 3, pp. 1953–1961, 2016.
- [53] M. Aneke and M. Wang, “Energy storage technologies and real life applications – a state of the art review,” *Applied Energy*, vol. 179, pp. 350–377, 2016. [Online]. Available: <https://www.sciencedirect.com/science/article/pii/S0306261916308728>
- [54] R. G. de Almeida and J. A. Pecas Lopes, “Participation of doubly fed induction wind generators in system frequency regulation,” *IEEE Transactions on Power Systems*, vol. 22, no. 3, pp. 944–950, 2007.
- [55] S. I. Abouzeid, Y. Guo, H.-C. Zhang, and X. Ma, “Improvements in primary frequency regulation of the grid-connected variable speed wind turbine,” *IET Renewable Power Generation*, vol. 13, no. 3, pp. 491–499, 2019. [Online]. Available: <https://ietresearch.onlinelibrary.wiley.com/doi/abs/10.1049/iet-rpg.2018.5187>
- [56] Y. Tang, C. Yang, Z. Yan, Y. Xue, and Y. He, “Coordinated control of a wind turbine and battery storage system in providing fast-frequency regulation and extending the cycle life of battery,” *Frontiers in Energy Research*, vol. 10, 2022. [Online]. Available: <https://www.frontiersin.org/articles/10.3389/fenrg.2022.927453>
- [57] J. Tan and Y. Zhang, “Coordinated control strategy of a battery energy storage system to support a wind power plant providing multi-timescale frequency ancillary services,” *IEEE Transactions on Sustainable Energy*, vol. 8, no. 3, pp. 1140–1153, 2017.
- [58] M. Świerczyński, D. I. Stroe, A. I. Stan, and R. Teodorescu, “Primary frequency regulation with li-ion battery energy storage system: A case study for denmark,” in *2013 IEEE ECCE Asia Downunder*, 2013, pp. 487–492.
-

-
- [59] V. Knap, S. K. Chaudhary, D.-I. Stroe, M. Swierczynski, B.-I. Craciun, and R. Teodorescu, "Sizing of an energy storage system for grid inertial response and primary frequency reserve," *IEEE Transactions on Power Systems*, vol. 31, no. 5, pp. 3447–3456, 2016.
- [60] M. Benini, S. Canevese, D. Cirio, and A. Gatti, "Battery energy storage systems for the provision of primary and secondary frequency regulation in Italy," in *2016 IEEE 16th International Conference on Environment and Electrical Engineering (EEEIC)*, 2016, pp. 1–6.
- [61] K. Stein, M. Tun, M. Matsuura, and R. Rocheleau, "Characterization of a fast battery energy storage system for primary frequency response," *Energies*, vol. 11, no. 12, 2018. [Online]. Available: <https://www.mdpi.com/1996-1073/11/12/3358>
- [62] X. Lu, K. Sun, J. M. Guerrero, J. C. Vasquez, L. Huang, and R. Teodorescu, "SOC-based droop method for distributed energy storage in DC microgrid applications," in *2012 IEEE International Symposium on Industrial Electronics*, 2012, pp. 1640–1645.
- [63] X. Li, Y. Huang, J. Huang, S. Tan, M. Wang, T. Xu, and X. Cheng, "Modeling and control strategy of battery energy storage system for primary frequency regulation," in *2014 International Conference on Power System Technology*, 2014, pp. 543–549.
- [64] C. Fang, Y. Tang, R. Ye, Z. Lin, Z. Zhu, B. Wen, and C. Ye, "Adaptive control strategy of energy storage system participating in primary frequency regulation," *Processes*, vol. 8, no. 6, 2020. [Online]. Available: <https://www.mdpi.com/2227-9717/8/6/687>
- [65] Y. Ota, H. Taniguchi, T. Nakajima, K. M. Liyanage, J. Baba, and A. Yokoyama, "Autonomous distributed V2G (vehicle-to-grid) considering charging request and battery condition," in *2010 IEEE PES Innovative Smart Grid Technologies Conference Europe (ISGT Europe)*, 2010, pp. 1–6.
- [66] D. C. Das, A. Roy, and N. Sinha, "Ga based frequency controller for solar thermal–diesel–wind hybrid energy generation/energy storage system," *International Journal of Electrical Power Energy Systems*, vol. 43, no. 1, pp. 262–279, 2012. [Online]. Available: <https://www.sciencedirect.com/science/article/pii/S0142061512002153>
- [67] M. Toge, Y. Kurita, and S. Iwamoto, "Supplementary load frequency control with storage battery operation considering SOC under large-scale wind power penetration," in *2013 IEEE Power Energy Society General Meeting*, 2013, pp. 1–5.
- [68] C.-F. Lu, "Dynamic modelling of battery energy storage system and application to power system stability," *IEE Proceedings - Generation, Transmission and*
-

-
- Distribution*, vol. 142, pp. 429–435(6), July 1995. [Online]. Available: <https://digital-library.theiet.org/content/journals/10.1049/ip-gtd.19951858>
- [69] S. K. Aditya and D. Das, “Load-frequency control of an interconnected hydro-thermal power system with new area control error considering battery energy storage facility,” *International Journal of Energy Research*, vol. 24, pp. 525–538, 2000.
- [70] A. Adrees, H. Andami, and J. V. Milanović, “Comparison of dynamic models of battery energy storage for frequency regulation in power system,” in *2016 18th Mediterranean Electrotechnical Conference (MELECON)*, 2016, pp. 1–6.
- [71] Z. Salameh, M. Casacca, and W. Lynch, “A mathematical model for lead-acid batteries,” *IEEE Transactions on Energy Conversion*, vol. 7, no. 1, pp. 93–98, 1992.
- [72] B. Lei, X. R. Li, J. Y. Huang, and S. J. Tan, “Droop configuration and operational mode setting of battery energy storage system in primary frequency regulation,” in *Renewable Energy and Environmental Technology*, ser. Applied Mechanics and Materials, vol. 448. Trans Tech Publications Ltd, 1 2014, pp. 2235–2238.
- [73] F. Calero, C. A. Cañizares, and K. Bhattacharya, “Dynamic modeling of battery energy storage and applications in transmission systems,” *IEEE Transactions on Smart Grid*, vol. 12, no. 1, pp. 589–598, 2021.
- [74] O. Tremblay and L.-A. Dessaint, “Experimental validation of a battery dynamic model for ev applications,” *World Electric Vehicle Journal*, vol. 3, no. 2, pp. 289–298, 2009. [Online]. Available: <https://www.mdpi.com/2032-6653/3/2/289>
- [75] J. Sun, D. Mitchell, M. Greuel, P. Krein, and R. Bass, “Averaged modeling of pwm converters operating in discontinuous conduction mode,” *IEEE Transactions on Power Electronics*, vol. 16, no. 4, pp. 482–492, 2001.
- [76] R. W. Erickson and D. Maksimović, “Converter dynamics and control,” in *Fundamentals of Power Electronics*, 3rd ed. Springer Cham, 2020, pp. XIX, 1084.
- [77] S. Chiniforoosh, J. Jatskevich, A. Yazdani, V. Sood, V. Dinavahi, J. A. Martinez, and A. Ramirez, “Definitions and applications of dynamic average models for analysis of power systems,” *IEEE Transactions on Power Delivery*, vol. 25, no. 4, pp. 2655–2669, 2010.
- [78] A. Davoudi and J. Jatskevich, “Parasitics realization in state-space average-value modeling of pwm dc–dc converters using an equal area method,” *IEEE Transactions on Circuits and Systems I: Regular Papers*, vol. 54, no. 9, pp. 1960–1967, 2007.
-

- [79] A. Davoudi, J. Jatskevich, and T. D. Rybel, "Numerical state-space average-value modeling of pwm dc-dc converters operating in dcm and ccm," *IEEE Transactions on Power Electronics*, vol. 21, no. 4, pp. 1003–1012, 2006.
- [80] V. Vorperian, "Simplified analysis of pwm converters using model of pwm switch. ii. discontinuous conduction mode," *IEEE Transactions on Aerospace and Electronic Systems*, vol. 26, no. 3, pp. 497–505, 1990.

Appendix A

- Standard IEEE bus-9 system

Table A.1: Terminal conditions of IEEE 9-bus system

Bus	Voltage (kV)	Phase angle (deg)	Active power (pu)	Reactive Power (pu)
1	17.1600	0.0000	0.7163	0.2791
2	18.4500	9.3507	1.6300	0.0490
3	14.1450	5.1420	0.8500	-0.1145

Table A.2: Transmission line characteristics of IEEE 9-bus system

Line		R (pu/m)	X (pu/m)	B (pu/m)
From bus	To bus			
4	5	0.0100	0.0680	0.0176
4	6	0.0170	0.0920	0.1580
5	7	0.0320	0.1610	0.3060
6	9	0.0390	0.1738	0.3580
7	8	0.0085	0.0576	0.1490
8	9	0.0119	0.1008	0.2090

Table A.3: Load characteristics of IEEE 9-bus system

Bus	P (pu)	Q (pu)
5	1.25	0.50
6	0.90	0.30
8	1.00	0.35

Table A.4: Synchronous generator parameters

Parameter	Value	Parameter	Value
Rated RMS line-to-neutral voltage	12.4707 kV	Base angular frequency	376.992 rad/s
Rated RMS line current	24.05 kA	Inertia constant	4s
Terminal voltage magnitude	1.045 pu	Mechanical friction and windage	0 pu
Armature resistance (R_a)	0.0046 pu	Potier reactance (X_p)	0.155 pu
Unsaturated reactance (X_d)	1.53 pu	Unsaturated transient reactance (X'_d)	0.256 pu
Unsaturated transient time (open) (T'_{do})	5.71 s	Unsaturated sub-transient reactance (X''_d)	0.215 pu
Unsaturated sub-transient time (open) (T''_{do})	0.06 s	Unsaturated reactance (X_q)	1.51 pu
Unsaturated sub-transient reactance (X''_q)	0.215 pu	Unsaturated sub-transient time (open) (T''_{qo})	0.06s
Unsaturated transient time (open) (T'_{qo})	0.5 s	Unsaturated transient reactance (X'_q)	0.424 pu

Table A.5: Exciter AC8B parameters

Parameter	Value	Parameter	Value
PID proportional gain (K_{PR})	10 pu	PID integral gain (K_{IR})	1.2 pu
PID derivative gain	0 pu	PID derivative time constant (K_{DR})	0.03 s
Regular gain (K_A)	1.0 pu	Regular time constant (T_A)	0.02 s
Maximum regulator output (VR_{max})	15 pu	Minimum regulator (VR_{min}) output	-5 pu
Field current limit	100	Exciter time constant (T_E)	0.7 s
Exciter constant related to field (K_E)	0.4	Field circuit commutating reactance (K_C)	0.4
Saturation at Efd1	0.39 pu	Exciter voltage for SE1	7 pu
Saturation at Efd2	3.7 pu	Exciter voltage for SE2	9.3 pu

Table A.6: Hydro governor parameters

Parameter	Value	Parameter	Value
Dead band value	0.00033 pu	Permanent droop (R_p)	0.2 pu
Maximum gate position (G_{max})	1.0 pu	Minimum gate position (G_{min})	0.0 pu
Maximum gate opening rate ($MXGTOR$)	1 pu/s	Maximum gate closing rate ($MXGTOR$)	1 pu/s
Pilot servo motor time constant (T_A)	0.05 pu	Gate servo time constant (T_C)	0.2 pu
Gate servomotor time constant (T_D)	0.2	Derivative gain (K_D)	0 pu

Table A.7: Hydro turbine parameters

Parameter	Value	Parameter	Value
Head at rated conditions	1.0 pu	Output power at rated conditions	1.0 pu
Gate position at rated conditions	1.0 pu	Rated no-load gate	0.05 pu
Water starting time (T_W)	2.0 s	Penstock head loss coefficient (f_p)	0.02 pu
Turbine damping constant (D)	0 pu		

Table A.8: Parameters of PPC

Parameter	Value
Upper limit on active power reference ($P_{max,1}$)	1 pu
Lower limit on active power reference ($P_{min,1}$)	0 pu
Upper limit on V/Q control (Q_{max})	0.477 pu
Lower limit on V/Q control (Q_{min})	-0.477 pu
Reactive power compensation gain (K_c)	0.04 pu
Active power PI controller proportional gain	0.1 pu
Active power PI controller integral gain	1 pu
Reactive power PI controller proportional gain	1.7 pu
Reactive power PI controller integral gain	5 pu